Titre: Title:	Modal Analysis of a Spinning Disk in a Dense Fluid as a Model for High Head Hydraulic Turbines
Auteur: Author:	Max Louyot
Date:	2019
Type:	Mémoire ou thèse / Dissertation or Thesis
Référence: Citation:	Louyot, M. (2019). Modal Analysis of a Spinning Disk in a Dense Fluid as a Model for High Head Hydraulic Turbines [Mémoire de maîtrise, Polytechnique Montréal]. PolyPublie. https://publications.polymtl.ca/3997/

URL de PolyPublie: PolyPublie URL:	https://publications.polymtl.ca/3997/
Directeurs de recherche: Advisors:	Frederick Gosselin
Programme: Program:	Génie aérospatial

POLYTECHNIQUE MONTRÉAL
affiliée à l'Université de Montréal

Modal Analysis of a Spinning Disk in a Dense Fluid as a Model for High Head Hydraulic Turbines

MAX LOUYOT
Département de génie mécanique

Mémoire présenté en vue de l'obtention du diplôme de *Maîtrise ès sciences appliquées*
Génie aérospatial

Août 2019

POLYTECHNIQUE MONTRÉAL
affiliée à l'Université de Montréal

Ce mémoire intitulé :

Modal Analysis of a Spinning Disk in a Dense Fluid as a Model for High Head Hydraulic Turbines

présenté par **Max LOUYOT**
en vue de l'obtention du diplôme de *Maîtrise ès sciences appliquées*
a été dûment accepté par le jury d'examen constitué de :

Jean-Yves TRÉPANIER, président
Frédérick P. GOSSELIN, membre et directeur de recherche
Stéphane ÉTIENNE, membre

DEDICATION

À mes parents, Isabelle et Frédéric.

ACKNOWLEDGEMENTS

Firstly, I would like to thank my research director Frédérick P. Gosselin for his continuous interest in my work and his help through these couple years in spite of an entire continent separating us. I would also like to thank my office mate Alexandre Couture for his smart suggestions, an always pleasant company, and the pastries of course.

Another warm thank to Bernd Nennemann for his quality supervision at Andritz Hydro and for helping me feel comfortable in the CFD group; group that I would also like to thank for their help in many different aspects of my work: Samer Afara, Maxime Gauthier, Matthieu Melot and Marine Heschung. For the same reason I would like to thank Melissa Fortin, Christine Monette and our european collegues Beat Horisberger and Olivier Braun.

My sincere acknowledgements to the MITACS Accelerate program and to Andritz Hydro for financing my research during this Master's. Lastly, I wish to thank École Polytechnique de Montréal and Université de Montréal for giving me the opportunity to go through this rich experience in the most pleasant context as a student.

RÉSUMÉ

Dans les turbines Francis de hautes chutes et dans les pompes-turbines en particulier, les Interactions Rotor Stator (RSI) sont une source d'excitation inévitable qui doit être prédite avec précision. Une connaissance pointue des caractéristiques dynamiques des turbines, notamment de la variation des fréquences naturelles du rotor en fonction de la vitesse de rotation et de la masse ajoutée de l'eau avoisinante, est essentielle à la prédiction de résonances potentielles et de l'amplification des vibrations résultantes. Dans ces machines, la couronne et la ceinture de la roue ainsi que les flasques supérieur et inférieur possèdent une structure similaire à un disque, ce qui donne lieu à l'apparition de modes diamétraux et à un phénomène de séparation des fréquences pour lequel aucune méthode de prédiction efficace n'existe à ce jour. Les méthodes d'Interactions Fluide-Structure (IFS) complètement couplées coûtant trop cher en temps de calcul, un modèle simplifié basé sur l'approche de force modale serait un outil puissant en terme de design et de prédiction de temps de vie de ces turbines.
Ce travail présente le développement d'un modèle analytique et d'un modèle de Mécanique des Fluides Numérique (CFD) pour les disques en rotation dans un fluide dense, permettant la prédiction précise de la séparation et du décalage des fréquences qui sont observés expérimentalement. De plus, une explication sur l'origine physique du phénomène de séparation des fréquences en est déduite. Ces modèles sont validés par comparaison avec des données expérimentales.

ABSTRACT

In high head Francis turbines and pump-turbines in particular, Rotor Stator Interactions (RSI) are an unavoidable source of excitation that needs to be predicted accurately. Precise knowledge of turbine dynamic characteristics, notably the variation of the rotor natural frequencies with rotation speed and added mass of the surrounding water, is essential to assess potential resonance and resulting amplification of vibrations. In these machines, the disk-like structures of the runner crown and band as well as the head cover and bottom ring give rise to the emergence of diametrical modes and a mode split phenomenon for which no efficient prediction method exists to date. Fully coupled Fluid-Structure Interaction (FSI) methods are too computationally expensive; hence, a simplified method based on the modal force approach would be a powerful tool for the design and expected life prediction of these turbines.

This work presents the development of both an analytical and a numerical Computational Fluid Dynamics (CFD) model for a rotating disk in dense fluid, which accurately predict the natural frequency split as well as the natural frequency drift that are observed empirically. Additionally, insight is given on the physical origin of the mode split phenomenon. These models are validated by comparison with experimental data.

TABLE OF CONTENTS

LIST OF TABLES

LIST OF FIGURES

LIST OF SYMBOLS AND ACRONYMS

1DOF	1-Degree Of Freedom
NDOF	N-Degrees Of Freedom
AVMI	Added Virtual Mass Incremental
NAVMI	Non-dimensional Added Virtual Mass Incremental
CFD	Computational Fluid Dynamics
FEA	Finite Element Analysis
FSI	Fluid-Structure Interactions
MMS	Memory Management System
RK4	Runge-Kutta method
RSI	Rotor-Stator Interaction
URANS	Unsteady Reynolds-Averaged Navier–Stokes

LIST OF APPENDICES

CHAPTER 1 INTRODUCTION

The design of modern hydroelectric turbines aims at near perfect efficiency while minimizing production costs. In this context, precise knowledge of the turbine dynamical characteristics, notably the variation of the rotor natural frequencies with rotation speed and added mass of the surrounding water, is essential to assess potential resonance and resulting amplification of vibrations. Turbine design requires fast and numerically efficient frequency identification methods taking into account these effects.

The manifold complexity of hydraulic turbines makes them subject to numerous physical effects. Resonance of structures coupled to excitation sources can lead to severe fatigue damage, that can result in the loss of hydraulic runner blades if it is not avoided (Coutu et al., 2004, 2008; Liu et al., 2016). Typically, the extra stresses due to daily start-stop cycles that turbines now undergo can initiate cracks in the blades (Huth, 2005; Trivedi and Cervantes, 2017). The intricacy of hydraulic turbine design and the numerous possible vibration sources in these machines make the runner reliability a challenging and critical criteria (Dörfler et al., 2012; Presas et al., 2019). In particular in high head Francis turbines and pump-turbines, Rotor-Stator Interaction (RSI) are an unavoidable source of excitation that needs to be predicted accurately (Dörfler et al., 2012; Walton and Tan, 2016) in order to ensure the designed geometry is suitable before its manufacturing.

Fully understanding the physics at stake is crucial in order to minimize the difficulties and delays experienced during the design stage of these machines. Critical rotation speeds of spinning structures trigger unstable regimes, such as flutter (Adams, 1987; Renshaw, 1998; Kim et al., 2000). Each structural mode can typically be stabilized by increasing the stiffness. The fluid filled spaces between rotor and casing also modify this threshold (Huang and Mote, 1995), especially with narrow gaps, like in hydraulic turbines. Additionally, the coupling between the acoustical and structural natural frequencies, the radial gap, the geometrical asymmetries, and the fluid rotation are all parameters upon which rotating structure stability relies (Kang and Raman, 2006a,b). The natural frequencies of runners are affected by equally numerous parameters including their rotational velocity and the influence of surrounding water (Egusquiza et al., 2016). Acoustical natural frequencies can decrease natural frequencies by up to 25% if coupling occurs (Bossio et al., 2017). Such frequencies are usually higher than rotation speeds for high head turbines. This review demonstrates the complexity of both runner physics and geometry. Hence, the untangling of physical phenomenon and relevant parameters of influence on runner natural frequencies requires a simplified approach.

If efficient frequency prediction methods exist for the dynamical response of low to medium head Francis runners (Coutu et al., 2008) and of Kaplan turbines (Soltani Dehkharqani et al., 2017, 2019), this is not the case for high head turbines and in particular pump-turbine runners. Vibration modeshapes of these runners are different due to the disk-like structures of the runner crown and band, which give rise to diametrical modes, as shown in Figure 1.1(a-b). Modeshapes of eigenfrequencies typically below 450 Hz are disk-like modes (Egusquiza et al., 2016), validating the disk representation of high head turbine runners for a large range of rotation speeds. Hence, the present work studies an idealized rotating plate in dense fluid. Beyond simplifying the rotor geometry to that of a disk, we can further idealize the problem with the following assumptions:

1. The rotation speed range considered for hydraulic turbine applications is low enough to neglect centrifugal forces in the disk.

2. For the selected potential flow approach, the fluid surrounding the disk is considered inviscid and adiabatic.

3. From the rotating disk reference frame, based on work from Poncet et al. (2005), the fluid is entrained to a solid-body motion at a mean velocity equal to a fraction of that of the disk.

4. The disk modes in water are the same as those of the disk in vacuum. This was confirmed by Kwak and Kim (1991) with the Rayleigh-Ritz method.

5. We consider small amplitude deformations of the disk in order to remain in the frame of linear perturbation analysis.

These assumptions allow us to orient our literature review.

Leissa (1969) compiles analytical solutions for annular plate modes and various boundary condition sets, using previous work from Southwell (1922) and Vogel and Skinner (1965) including geometries and conditions of particular interest for the present work.

Submerged structure resonance frequencies are shifted by the surrounding water effect (Liang et al., 2007; Østby et al., 2019). Part of the fluid vibrates with the structure, adding mass to the system. The plate rotation in water additionally triggers a particular resonance mechanism, first described by Kubota and Ohashi (1991): unlike in air, forward and backward travelling waves on the disk surface trigger the so-called mode split, as a mode can be excited with two different frequencies, as shown in Figure 1.1(c-d). However, there is little information on the physical phenomenon itself. Presas et al. (2014, 2015, 2016) along with Valentín

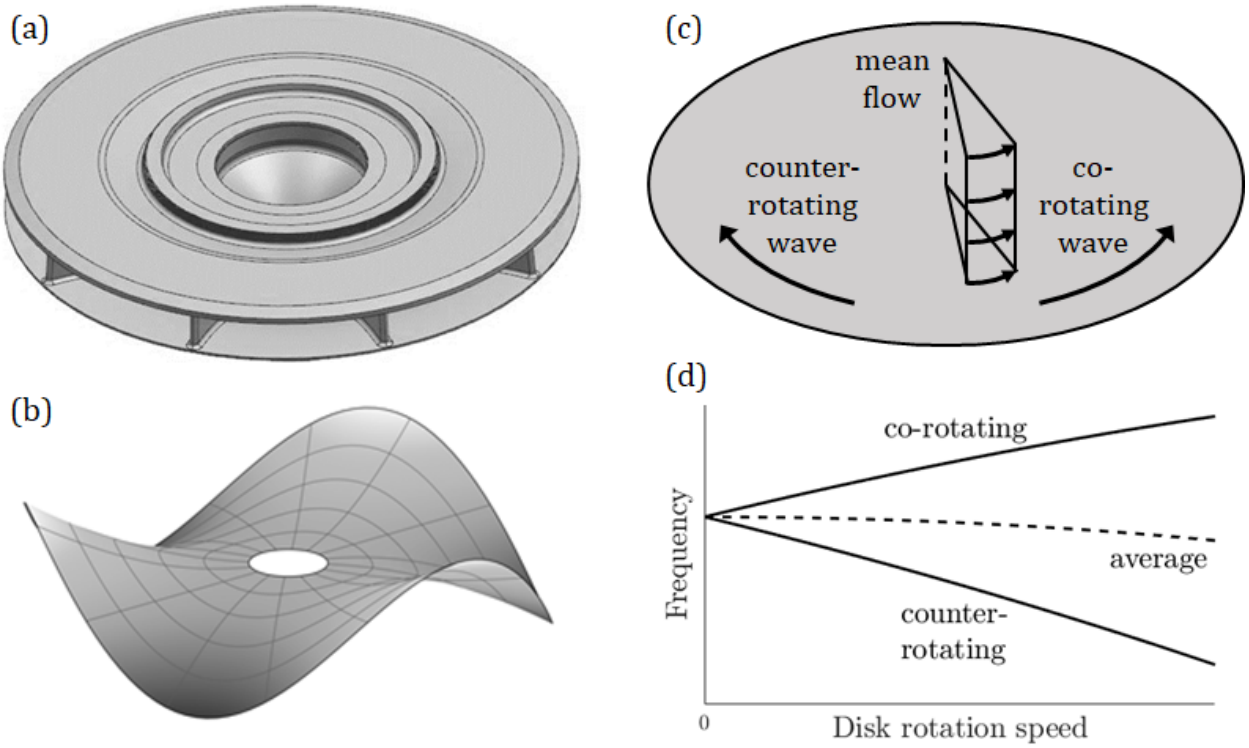

Figure 1.1 (a) A pump-turbine runner geometry. (b) High head Francis and pump-turbine runners have disk-like modeshapes, characterized by their number n of nodal diameters ($n = 3$ is presented). (c) Each disk mode is composed of a co-rotating and a counter-rotating wave, with respect to the fluid rotation relative to the disk. (d) Co- and counter-rotating wave frequencies evolve with the disk rotation speed in dense fluid: the split between the two increases, while the average value decreases.

et al. (2014) analytically and experimentally studied the natural frequencies of a submerged and confined rotating disk, as well as the influence of the rotation speed and of the axial gap length. Their experimental setup consists of a rotating disk excited with a piezoelectric patch, surrounded by air or water in a fully-rigid casing. The disk response was measured with accelerometers mounted on its surface, allowing the detection of the first structural modeshapes and associated frequencies. They showed that reducing the axial gap increases the mode split effect and decreases natural frequencies.

Various methods exist to study the vibrations of rotating structures. While considering coupled structural eigenmodes may prove close to reality, it can also be difficult to implement. Modal analysis only deals with independent modes, greatly simplifying the problem to solve. Ahn and Mote (1998) analytically studied the steady-state modal response of an excited rotating disk, and identified the modes linked to forward and backward travelling waves,

along with their associated frequencies. Renshaw et al. (1994) identified the ratio of the fluid and plate densities to be one of the main influencing parameters: mode split arises when the structure interacts with dense fluids such as water. Kwak and Kim (1991) and Amabili and Kwak (1996) analytically analyzed stationary circular plates coupled with water. They used the assumed mode approximation and worked with a potential flow. The assumed shape of the potential function must satisfy the boundary conditions; it provides spatial and temporal information on the velocity field. Then, assessing the Non-dimensional Added Virtual Mass Incremental (NAVMI) factor from the potential flow and imposed modeshape, they linked the natural frequency in vacuum to that in dense fluid. This factor represents the ratio between reference kinetic energies of the disk and fluid. Amabili et al. (1996) performed the same analysis on standing annular plates, proving its applicability to the disk considered in our work. The model developed by Presas et al. (2016) includes the relative rotation between the fluid and disk, which gives rise to mode split. It expresses the axial deformation at a characteristic radius r_0, and assumes that natural frequencies can be determined only from the disk dynamical information at $r = r_0$. The axial gap dimensions are taken into account through the boundary conditions. Unfortunately, all of these models still lack an exhaustive understanding of the physical nature of mode split and present a non-negligible relative error on the frequency predictions.

Analytical solutions cannot be established for hydraulic turbine complex geometries. Numerical FSI models using Finite Element Analysis (FEA) are powerful tools for the structural design analysis of these machines (Dompierre and Sabourin, 2010; Hübner et al., 2016). This method is applicable to natural frequency prediction of standing circular plates (Hengstler, 2013), disk-fluid-disk systems, rotor-stator systems (Specker, 2016; Weder et al., 2016, 2019), and rotating disks in fluid (Weber and Seidel, 2015). This shows that the application range of numerical FSI is extremely broad, and widely used to deal with disk frequency prediction. However, these fully-coupled simulations are computationally expensive (Hübner et al., 2016; Nennemann et al., 2016; Biner, 2017) and are not a convenient tool to evaluate runner natural frequencies in flow in the preliminary design stage (Weber and Seidel, 2015). They also present stability issues when the fluid-to-structure density ratio increases (Wong et al., 2013), typically when the fluid is water. Therefore, a simplified approach to model high head Francis and pump-turbines would be a powerful tool in the scope of our study. Several authors suggested using a faster approach than fully-coupled FSI, such as transient flow (Soltani Dehkharqani et al., 2017) or structural-acoustical methods (Valentín et al., 2016; Escaler and De La Torre, 2018). But because of both its simplicity and efficiency for submerged and confined rotating disks, the most promising alternative is a modal force approach (Nennemann et al., 2016; Presas et al., 2016; Biner, 2017), for which an arbitrary number of

modes considered separately are imposed on the disk surface. A time discretization of structural equations allows the computation of the displacement according to the surrounding fluid parameters and pressure field obtained with CFD. In order to numerically capture the mode split on rotating submerged disks, our work builds on the 1-degree of freedom (1DOF) oscillator modal force CFD model developed by Monette et al. (2014) and Nennemann et al. (2016). This model was originally used to predict added stiffness and damping of runner blades in flowing water.

Here we present the development of both an analytical modal analysis and a modal force CFD approach for rotating disks in dense fluid, which accurately predict the natural frequency split and drift that are observed experimentally by Presas et al. (2016) and Weder et al. (2019). Insight into the physical origin of the mode split is also given. Both models are validated by comparison with available experimental data.

CHAPTER 2 METHODOLOGY

In this section we detail the development of the structural and fluid equations leading to the analytical modal analysis, and the modal force CFD approaches. The disk material, geometry and rotation speed, as well as the fluid and casing properties are taken into account. The radial gap is only considered in the numerical model.

The disk is a rotating annular plate of density ρ_D, outer radius a, inner radius b, thickness h and angular speed Ω_D in the stationary reference frame. We use the cylindrical coordinates (r, θ, z) in the stationary reference frame, and the origin is taken at the center of the disk. The rigid casing of height $H_{up} + H_{down}$ is filled with a liquid of density ρ_F. The gap between the disk and the top of the casing is of length H_{up}, while the gap between the disk and the bottom of the casing is of length H_{down}. Figure 2.1 presents the modeled geometry.

2.1 Structural model

Let us first establish the structural equations upon which rely both analytical and numerical methods. According to linear classical plate theory, the vertical displacement w of an annular plate is given by Leissa (1969) as

$$D\nabla^4 w + \rho_D h \frac{\partial^2 w}{\partial t^2} = P(r, \theta, t)\,, \tag{2.1}$$

where t is the elapsed time, $P(r, \theta, t)$ is the pressure field applied to the plate, $\nabla^4 = \nabla^2\nabla^2$ with ∇^2 the Laplacian operator, and

$$D = \frac{Eh^3}{12(1-\nu^2)}\,, \tag{2.2}$$

is the disk flexural rigidity, where E is Young's modulus and ν is Poisson's ratio of the disk material, most likely stainless steel for hydraulic turbine applications. We introduce n (respectively s) as the number of nodal diameters (respectively circles) of the considered mode, and its associated modeshape in vacuum W_n. In order to determine W_n, we introduce the parameter k_n defined as

$$k_n^4 = \frac{\rho_D h \omega_v^2}{D}\,, \tag{2.3}$$

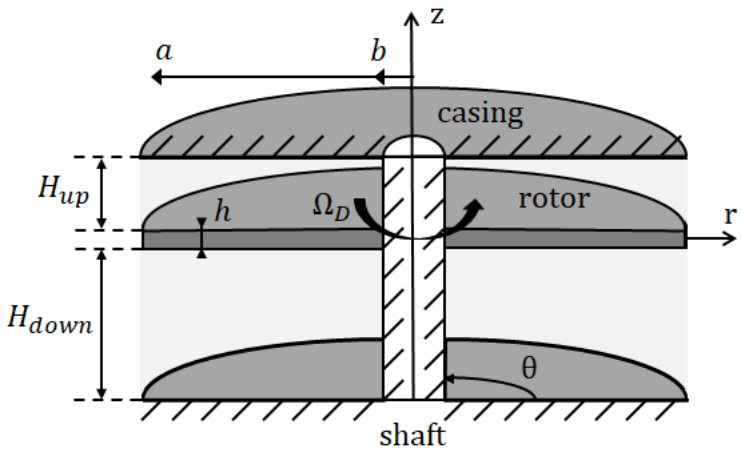

Figure 2.1 Studied geometry in §2.1 and §2.2: the disk with angular speed Ω_D, outer radius a, inner radius b and thickness h is confined in a rigid casing of height $H_{up} + H_{down}$, filled with water. The disk is clamped to the shaft on its inner radius and free outside.

which yields the information on the natural angular frequency in vacuum ω_v. Leissa (1969) provides the boundary conditions for the free-clamped annular plate:

$$W_n(r,\theta)\Big|_{r=b} = 0\,, \qquad \frac{\partial W_n(r,\theta)}{\partial r}\bigg|_{r=b} = 0\,, \tag{2.4}$$

$$V_r(r,\theta)\Big|_{r=a} = 0\,, \qquad M_r(r,\theta)\Big|_{r=a} = 0\,, \tag{2.5}$$

where V_r is the radial Kelvin-Kirchhoff edge reaction and M_r is the bending moment:

$$V_r = -D\left[\frac{\partial}{\partial r}(\nabla^2 W_n(r,\theta)) + (1-\nu)\frac{1}{r}\frac{\partial^2}{\partial\theta\partial r}\left(\frac{1}{r}\frac{\partial W_n(r,\theta)}{\partial\theta}\right)\right], \tag{2.6}$$

$$M_r = -D\left[\frac{\partial^2 W_n(r,\theta)}{\partial r^2} + \nu\left(\frac{1}{r}\frac{\partial W_n(r,\theta)}{\partial r} + \frac{1}{r^2}\frac{\partial^2 W_n(r,\theta)}{\partial\theta^2}\right)\right]. \tag{2.7}$$

For annular plates, the modeshape for a single mode is expressed as

$$W_n(r,\theta) = \psi_n(r)\, e^{in\theta}\,, \tag{2.8}$$

where

$$\psi_n(r) = A_n J_n(k_n r) + B_n Y_n(k_n r) + C_n I_n(k_n r) + D_n K_n(k_n r)\,, \tag{2.9}$$

where J_n, Y_n, I_n, K_n are the Bessel functions of first and second kinds, and the modified Bessel functions of first and second kinds respectively, and A_n, B_n, C_n, D_n are coefficients determined with the boundary conditions within a multiplying factor (Leissa, 1969). It should be noted

that the complex conjugate part is omitted in order to lighten the equations.

Substituting Eqs. (2.8-2.9) in Eqs. (2.4-2.5) results in a problem of the form:

$$\mathbf{M} \cdot \mathbf{X_n} = \begin{bmatrix} a_i & \cdots & d_i \\ \vdots & \ddots & \vdots \\ a_{iv} & \cdots & d_{iv} \end{bmatrix} \cdot \begin{bmatrix} A_n \\ B_n \\ C_n \\ D_n \end{bmatrix} = \mathbf{0}\,, \tag{2.10}$$

where the matrix coefficients a_i ... d_{iv} are given by the developed boundary conditions. We then have $det(\mathbf{M}) = 0$ as a necessary condition for the system to be solved. Solving $det(\mathbf{M}) = 0$ has an infinite number of solutions which correspond to the values of k for any number of nodal circles s. This cannot be solved analytically, and k must be evaluated numerically. After eliminating the trivial solution $k = 0$ and moving upward, the j^{th} solution that nullifies $det(\mathbf{M})$ corresponds to $s = j-1$. Then, in order to close the system of equations, we arbitrarily choose the value of A_n and then solve the system to get the values of B_n, C_n, D_n, and hence the associated modeshape. These modeshapes naturally form an orthogonal base, and we additionally choose A_n to make it orthonormal.

Let us apply the Galerkin method to the disk structure. The displacement is approximated with a discrete sum:

$$w(r,\theta,t) \approx w_N(r,\theta,t) = \sum_{j=1}^{N} \phi_j(r,\theta) q_j(t)\,, \tag{2.11}$$

where N is the number of modes of different nodal diameters considered, ϕ are test functions that satisfy the boundary conditions and q are the generalized coordinates. Here, the test functions are chosen to correspond to the orthonormal modeshapes: $\phi_j(r,\theta) = W_j(r,\theta)$ defined in Eq. (2.8). Calculation shows that this choice implies $\nabla^4 W_j = k_j^4 W_j$. Hence, substituting w with w_N in Eq. (2.1) leads to

$$D\nabla^4 w_N + \rho_D h \frac{\partial^2 w_N}{\partial t^2} - P(r,\theta,t) = \mathcal{R}\,, \tag{2.12}$$

where $\mathcal{R}$ is the residual. Expanding the sum of Eq. (2.11):

$$\sum_{j=1}^{N} \Big[\rho_D h \ddot{q}_j(t) + D k_j^4 q_j(t)\Big] W_j(r,\theta) - P(r,\theta,t) = \mathcal{R}\,, \tag{2.13}$$

where $\ddot{q}_j = \partial^2 q_j / \partial t^2$. According to the Galerkin method:

$$\int_{r=b}^{a} \int_{\theta=0}^{2\pi} \mathcal{R} W_i(r,\theta)\, r dr d\theta = 0 \;\forall i \in [1, N]\,. \tag{2.14}$$

Let us recall that because the modes form an orthonormal base,

$$\int_{r=b}^{a}\int_{\theta=0}^{2\pi} W_i(r,\theta)W_j(r,\theta)r\,dr d\theta = 2\pi(a^2-b^2)\delta_{ij}\,, \tag{2.15}$$

where δ_{ij} is the Kronecker symbol. Therefore, multiplying Eq. (2.13) by W_i and integrating over the annular plate surface, we obtain

$$2\pi(a^2-b^2)\sum_{j=1}^{N}\Big[\rho_D h\ddot{q_j}(t) + Dk_j^4 q_j(t)\Big]\delta_{ij} = \widetilde{P}_i(t)\,, \tag{2.16}$$

where

$$\widetilde{P}_i(t) = \int_{r=b}^{a}\int_{\theta=0}^{2\pi} P(r,\theta,t)W_i(r,\theta)\,r dr d\theta\,. \tag{2.17}$$

Let us recall that this is true for any number of considered modes N chosen arbitrarily. Observing that the equations from the obtained system are decoupled, we can then generalize for any chosen mode:

$$2\pi(a^2-b^2)\Big[\rho_D h\ddot{q_n}(t) + Dk_n^4 q_n(t)\Big] = \widetilde{P}_n(t)\,, \tag{2.18}$$

where n is the number of nodal diameters. Hence, any point on the disk can be assimilated to a 1DOF mass-spring system with vertical motion for any given mode. The vertical displacement w of this point follows

$$M_s\ddot{w}(t) + K_s w(t) = \widetilde{P}_n(t)\,, \tag{2.19}$$

where $M_s = 2\pi(a^2-b^2)\rho_D h$ and $K_s = 2\pi(a^2-b^2)Dk^4$ are the modal structural mass and stiffness respectively. It can be seen that the structural modal mass only depends on the mass and geometry of the disk, regardless of the selected mode; while the structural modal stiffness depends through k on the number of nodal diameters and circles of the mode. The disk natural angular frequency in vacuum can be assessed with Eq. (2.19):

$$\omega_v = \sqrt{\frac{K_s}{M_s}} = k^2\sqrt{\frac{D}{\rho_D h}}\,. \tag{2.20}$$

2.2 FSI analytical model

In this section we develop an analytical model based on modal analysis, for the prediction of rotating disk natural frequencies. Let us recall that modeshapes are considered identical in air and in water. Fluid above and below the disk is taken into account, but not on the side: the radial gap between the disk and casing is considered null.

At this point, because k is known, we have an expression for any annular plate modeshape given by Eq. (2.8), and associated angular frequency in vacuum given by Eq. (2.20). As we only consider a single mode with n nodal diameters, we have $N = 1$ with respect to Eq. (2.11), which translates into

$$w(r, \theta, t) = W_n(r, \theta) g(t) \,, \tag{2.21}$$

with

$$g(t) = e^{i\omega t} \,, \tag{2.22}$$

and ω is the actual angular frequency of the structure for the considered mode.

We consider the fluid velocity $\mathbf{V}$ in the surrounding fluid, the form of which is assumed to be the sum of a mean flow component $\mathbf{V_0}$, associated with the rotating solid body motion, and of an oscillatory component $\mathbf{v}$, associated with the transverse disk motion:

$$\mathbf{V}(r, \theta, z, t) = \mathbf{V_0}(r) + \mathbf{v}(r, \theta, z, t) \,. \tag{2.23}$$

The solid body motion is described by

$$\mathbf{V_0} = \begin{cases} 0 \\ (1 - K) r \Omega_D \\ 0 \end{cases} \,, \tag{2.24}$$

in the cylindrical reference frame, where K is the average entrainment coefficient, the value of which will be discussed in §3.2. This coefficient verifies $K = \Omega_F / \Omega_D$, where Ω_F is the fluid angular speed in the stationary reference frame.

We associate the oscillatory component $\mathbf{v}$ to the flow potential Φ:

$$\mathbf{v} = \nabla \Phi \,, \tag{2.25}$$

where we assume the shape of Φ to be

$$\Phi(r, \theta, z, t) = \phi(r, z) e^{in\theta} \dot{g}(t) \,, \tag{2.26}$$

where $\dot{g} = dg/dt$, g is defined in Eq. (2.22) and ϕ has to be determined. By convention, $n > 0$ (respectively $n < 0$) characterizes co-rotating waves (respectively counter-rotating

waves) relative to the rotating disk. This flow obeys the Laplace equation, which implies

$$\nabla^2\Phi = \frac{\partial^2\Phi}{\partial r^2} + \frac{1}{r}\frac{\partial\Phi}{\partial r} + \frac{1}{r^2}\frac{\partial^2\Phi}{\partial\theta^2} + \frac{\partial^2\Phi}{\partial z^2} = 0\,. \tag{2.27}$$

Substituting Φ for its expression in Eq. (2.26) yields the equation solved by ϕ:

$$\frac{\partial^2\phi}{\partial r^2} + \frac{1}{r}\frac{\partial\phi}{\partial r} - \frac{n^2}{r^2}\phi + \frac{\partial^2\phi}{\partial z^2} = 0\,. \tag{2.28}$$

As the fluid must remain inside the defined domain, its radial velocity is null at both the inner and outer radii:

$$\left.\frac{\partial\phi}{\partial r}\right|_{r=b} = 0\,, \qquad \left.\frac{\partial\phi}{\partial r}\right|_{r=a} = 0\,. \tag{2.29}$$

Additionally, the non-penetration boundary conditions on the top and bottom casing and disk surfaces imply

$$\left.\frac{\partial\phi}{\partial z}\right|_{z=H_{up}} = 0\,, \qquad \left.\frac{\partial\phi}{\partial z}\right|_{z=H_{down}} = 0\,, \tag{2.30}$$

$$\left.\frac{\partial\phi}{\partial z}\right|_{z=0} = \frac{Dw}{Dt} = \frac{\partial w}{\partial t} + \frac{\mathrm{V}_{0,\theta}}{r}\frac{\partial w}{\partial\theta}\,, \tag{2.31}$$

where D/Dt is the material derivative, and $\mathrm{V}_{0,\theta}$ is the tangential velocity in the fluid reference frame. Then, replacing w in Eq. (2.31) by its expression given by Eqs. (2.8, 2.21) yields

$$\left.\frac{\partial\phi}{\partial z}\right|_{z=0} = \left(1 + \frac{n}{\omega}\frac{\mathrm{V}_{0,\theta}}{r}\right)\psi_n(r)\,. \tag{2.32}$$

Substituting the tangential velocity $\mathrm{V}_{0,\theta}$, given by Eq. (2.24), finally provides

$$\left.\frac{\partial\phi}{\partial z}\right|_{z=0} = \left(1 + \frac{n\Omega_{D/F}}{\omega}\right)\psi_n(r)\,, \tag{2.33}$$

where $\Omega_{D/F} = \Omega_D - \Omega_F = (1-K)\Omega_D$ is the disk angular speed with respect to the fluid.

Similarly to Amabili et al. (1996), we introduce the Hankel transform based on Bessel functions to write the potential flow as

$$\phi(r,z) = \int_0^\infty \xi[B(\xi)e^{-\xi z} + C(\xi)e^{\xi z}]J_n(\xi r)\,d\xi\,, \tag{2.34}$$

where the functions $B(\xi), C(\xi)$ are to be determined with the boundary conditions. We also introduce the non-dimensional variables $\hat{r} = r/a$, $\eta = r\xi$, $\hat{H}_{up} = H_{up}/a$, $\hat{H}_{down} = H_{down}/a$,

$\hat{z} = z/a$ and $\tau = t/t_0$, where $t_0 = \sqrt{\rho_D h/D}$ is a reference time. The condition on the top casing surface in Eq. (2.32) gives

$$B(\eta)e^{-\eta\hat{H}_{up}} - C(\eta)e^{\eta\hat{H}_{up}} = 0\,, \tag{2.35}$$

Then isolating $C(\eta)$ and substituting its expression in Eq. (2.33) yields

$$\int_0^\infty \eta\Big[\eta B(\eta)\Big(1 - e^{-2\eta\hat{H}_{up}}\Big)\Big] J_n(\eta\hat{r})\, d\eta = -a^3\Big(1 + \frac{n\Omega_{D/F}}{\omega}\Big)\psi_n(\hat{r})\,. \tag{2.36}$$

Upon applying the inverse Hankel transform we obtain

$$\eta B(\eta)\Big(1 - e^{-2\eta\hat{H}_{up}}\Big) = -a^3\Big(1 + \frac{n\Omega_{D/F}}{\omega}\Big)\int_{b/a}^1 \hat{r}\,\psi_n(\hat{r}) J_n(\eta\hat{r})\, d\hat{r}\,. \tag{2.37}$$

This new integral can be evaluated numerically. Ultimately, this allows us to calculate:

$$\eta[B(\eta) + C(\eta)] = -a^3\Big(1 + \frac{n\Omega_{D/F}}{\omega}\Big)\Big(\frac{1 + e^{-2\eta\hat{H}_{up}}}{1 - e^{-2\eta\hat{H}_{up}}}\Big)\int_{b/a}^1 \hat{r}\,\psi_n(\hat{r}) J_n(\eta\hat{r})\, d\hat{r}\,. \tag{2.38}$$

And replacing this expression in Eq. (2.34) gives the expression of the potential flow in the fluid volume:

$$\phi_{up}(\hat{r},\hat{z}) = -a\omega\Big(1 + \frac{n\Omega_{D/F}}{\omega}\Big)\int_0^\infty H(\eta) J_n(\eta\hat{r})\Big[\frac{e^{-\eta\hat{z}} + e^{\eta(\hat{z}-2\hat{H}_{up})}}{1 - e^{-2\eta\hat{H}_{up}}}\Big]\, d\eta\,, \tag{2.39}$$

$$\phi_{down}(\hat{r},\hat{z}) = -a\omega\Big(1 + \frac{n\Omega_{D/F}}{\omega}\Big)\int_0^\infty H(\eta) J_n(\eta\hat{r})\Big[\frac{e^{-\eta\hat{z}} + e^{\eta(\hat{z}-2\hat{H}_{down})}}{1 - e^{-2\eta\hat{H}_{down}}}\Big]\, d\eta\,, \tag{2.40}$$

where

$$H(\eta) = \int_{b/a}^1 \hat{r}\,\psi_n(\hat{r}) J_n(\eta\hat{r})\, d\hat{r}\,. \tag{2.41}$$

The perturbation fluid velocity magnitude depends on the rotation speed and frequency of the considered mode; while the velocity field shape only depends on the modeshape and geometrical properties of the domain. Evaluating Eqs. (2.39-2.40) at the disk surface $\hat{z} = 0^+$ yields

$$\phi_{up}(\hat{r},0) = -a\omega\Big(1 + \frac{n\Omega_{D/F}}{\omega}\Big)\int_0^\infty H(\eta) J_n(\eta\hat{r}) G_{up}(\eta)\, d\eta\,, \tag{2.42}$$

$$\phi_{down}(\hat{r},0) = -a\omega\Big(1 + \frac{n\Omega_{D/F}}{\omega}\Big)\int_0^\infty H(\eta) J_n(\eta\hat{r}) G_{down}(\eta)\, d\eta\,, \tag{2.43}$$

where

$$G_{up}(\eta) = \frac{1 + e^{-2\eta\hat{H}_{up}}}{1 - e^{-2\eta\hat{H}_{up}}}\,, \qquad G_{down}(\eta) = \frac{1 + e^{-2\eta\hat{H}_{down}}}{1 - e^{-2\eta\hat{H}_{down}}}\,, \tag{2.44}$$

so that H only depends on the mode and on the disk dimensions, and G_{up}, G_{down} only depend on the disk and casing dimensions.

In order to assess the influence of the surrounding fluid on the natural frequencies of the structure, we calculate the Added Virtual Mass Incremental (AVMI) factor β, which links natural frequencies in vacuum to natural frequencies in the considered fluid (Kwak and Kim, 1991; Amabili et al., 1996):

$$\frac{\omega}{\omega_v} = \frac{1}{\sqrt{1+\beta}}\,. \tag{2.45}$$

The AVMI factor is expressed as the ratio between the reference kinetic energy of the surrounding fluid E_F to the reference kinetic energy of the disk E_D. On the one hand, both the reference kinetic energies of the above and below fluid must be considered:

$$E_F = -\frac{1}{2}\rho_F a^2 \psi_\theta \Big(1 + \frac{n\Omega_{D/F}}{\omega}\Big) \int_{b/a}^{1} \Big[\phi_{down}(\hat{r},0) + \phi_{up}(\hat{r},0)\Big] \psi_n(\hat{r}) \hat{r}\, d\hat{r}\,, \tag{2.46}$$

where $\psi_\theta = 2\pi$ if $n = 0$ and $\psi_\theta = \pi$ otherwise, as results from the integration over θ. Then replacing the flow potentials by their known expressions Eqs. (2.42-2.43):

$$E_F = \frac{1}{2}\rho_F a^3 \psi_\theta \Big(1 + \frac{n\Omega_{D/F}}{\omega}\Big)^2 \times \int_{b/a}^{1}\int_{0}^{\infty} H(\eta) J_n(\eta\hat{r}) \Big[G_{down}(\eta) + G_{up}(\eta)\Big]\, d\eta\, \psi_n(\hat{r}) \hat{r}\, d\hat{r}\,. \tag{2.47}$$

On the other hand, the reference kinetic energy of the disk is

$$E_D = \frac{1}{2}\rho_D a^2 \psi_\theta h \int_{b/a}^{1} \psi_n(\hat{r})^2 \hat{r}\, d\hat{r}\,. \tag{2.48}$$

Therefore, the AVMI factor can be expressed as

$$\beta = \frac{E_F}{E_D} = \rho_F a \Big(1 + \frac{n\Omega_{D/F}}{\omega}\Big)^2 \times \frac{\int_{b/a}^{1}\int_{0}^{\infty} H(\eta) J_n(\eta\hat{r}) \Big[G_{down}(\eta) + G_{up}(\eta)\Big]\, d\eta\, \psi_n(\hat{r}) \hat{r}\, d\hat{r}}{\rho_D h \int_{b/a}^{1} \psi_n(\hat{r})^2 \hat{r}\, d\hat{r}}\,. \tag{2.49}$$

At this point we can see that β depends on ω when the disk is rotating. Let us call β_0 the

expression of the AVMI factor when there is no rotation:

$$\beta_0 = \beta \Big|_{\Omega_{D/F}=0} . \tag{2.50}$$

Hence,

$$\beta = \left(1 + \frac{n\Omega_{D/F}}{\omega}\right)^2 \beta_0 , \tag{2.51}$$

where β_0 only depends on the fluid, casing and disk geometry and material parameters, and the $n\Omega_{D/F} = n(1-K)\Omega_D$ term yields the influence of the disk rotation. Both parts depend on the considered mode.

Manipulating the implicit expression given by Eq. (2.45) of the natural frequency as a function of β, we can write the following explicit formulation for the modal analytical prediction of rotating and submerged disk natural angular frequencies:

$$\omega = \frac{\sqrt{(\beta_0+1)\omega_v^2 - \beta_0(n\Omega_{D/F})^2} - n\beta_0\Omega_{D/F}}{\beta_0 + 1} . \tag{2.52}$$

Some integral terms in the developed expression of β_0 need to be determined numerically. MATLAB was chosen to implement the method developed in this section. Results for various sets of geometries and modes can be obtained in only a few seconds.

2.3 FSI numerical model

In this section we develop a numerical model using results of modal analysis and CFD, for the prediction of rotating disks natural frequencies. The model can be applied to arbitrarily complex structures, taking into account the radial gap between the disk and the side walls for instance. The aim for this model is purely to predict natural frequencies using solely ANSYS CFX, without the structure coupling module. Hydraulic turbine efficiency assessment is out of the scope of this study.

The oscillating disk in vacuum presents two repeated frequencies for each mode, associated with a co- and counter-rotating wave (Ahn and Mote, 1998). With respect to Eq. (2.11), we need to consider $N = 2$ in order to capture both waves. If the disk is rotating in dense fluid, each wave has its own angular frequency, ω_+ and ω_- respectively. The pair of counter-phased modes $W_{n,c}$ and $W_{n,s}$ that we consider is called *companion modes*[1] (an example is given in Figure 2.2), where the subscripts c and s refer to the cosine and sine forms of the mode

[1] $W_s(r,\theta) = W_c(r,\theta - \pi/2n)$

respectively:

$$W_c(r,\theta) = \psi_n(r)\,\cos(n\theta)\,, \tag{2.53}$$

$$W_s(r,\theta) = \psi_n(r)\,\sin(n\theta)\,. \tag{2.54}$$

Replacing the solution of the previous section, the vertical displacement is now given by

$$w(r,\theta,t) = W_c(r,\theta)q_c(t) + W_s(r,\theta)q_s(t)\,, \tag{2.55}$$

where q_c and q_s are the two unknowns to be determined by coupling CFD with a mass-spring system, namely the two generalized coordinates of the 2DOF problem. Because the mass-spring Eq. (2.19) solved by w is linear, it is equivalent to the following system solved by q_c and q_s:

$$\ddot{q_c}(t) + \omega^2 q_c(t) = \frac{F_c(t)}{M_s}\,,\ \text{where } F_c(t) = \int_{r=b}^{a}\int_{\theta=0}^{2\pi} P(r,\theta,t)W_c(r,\theta)\,r dr d\theta\,, \tag{2.56}$$

$$\ddot{q_s}(t) + \omega^2 q_s(t) = \frac{F_s(t)}{M_s}\,,\ \text{where } F_s(t) = \int_{r=b}^{a}\int_{\theta=0}^{2\pi} P(r,\theta,t)W_s(r,\theta)\,r dr d\theta\,. \tag{2.57}$$

The modal forces F_c and F_s are the projections of the pressure fields on the respective modeshapes W_c and W_s. The angular frequency ω and the modal mass M_s are unchanged because they only depend on the structural properties. Water effects are taken into account through the modal force. Solving these equations with CFD provides time signals for $q_c(t)$ and $q_s(t)$, from which the angular frequencies ω_+ and ω_- can be deduced.

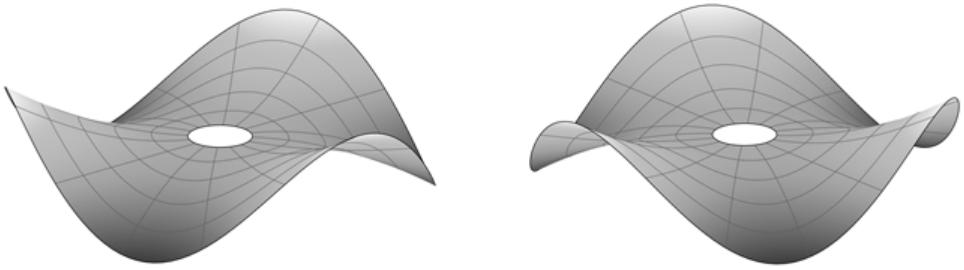

Figure 2.2 Companion modes $n = 3$, $s = 0$ for an annular plate

The CFD method developed in this section was implemented with Ansys CFX 18.2. The fluid equations are solved by Ansys CFX itself, while the disk displacement according to the imposed modeshape is implemented with custom user CEL functions and Fortran routines (see Figure 2.3). Ansys CFX performs Unsteady Reynolds-Averaged Navier–Stokes (URANS) calculations with a second order backward Euler transient scheme. We use CFX

`High resolution` advection scheme, which means the code tries second order where possible and reduces to first order where convergence is compromised. More details on CFX model implementation can be found in Ansys CFX User's Manual. For a mode with n nodal diameters, only a fraction $1/n$ of the actual geometry is represented and periodic boundary conditions are applied consequently. The fluid domain mesh (presented in Figure 2.4) is composed of approximately 10^4–10^5 cubic hexagonal elements, depending on the studied mode. As the fluid rotates with the disk, their are higher gradients for smaller axial gaps, hence the finer mesh above the disk. This coarse mesh is sufficient for our simulations because mode split is an inviscid fluid phenomenon, hence it is not influenced by viscous effects in the boundary layer. Mesh convergence was ensured, calculating a 1.96% frequency relative error with finer meshes (refinement factor of 2 in all three dimensions). The radial gap is considered in this model.

The model first requires input parameters. The cosine and sine form of the modeshape are established using Eq. (2.8), and normalized according to Eq. (2.15). The Bessel functions are approximated with polynomials. The modal mass and rigidity of the structure are determined from our structural analysis in §2.1, using the disk material properties: $M_s = \rho_D h$ and $K_s = Dk^4 = M_s\omega_v^2$. The surrounding dense fluid, typically water for hydraulic turbine applications, is considered compressible to avoid numerical instability issues due to pressure wave propagation, as indicated in the guidelines provided by Ansys. Turbulence is represented with a k-ϵ model. $Y^+ > 30$ in the mesh validates this model. The time step duration Δt is paramount to achieve numerical stability in this case of high fluid-solid density ratio (Wong et al., 2013). Typically, for steel runners in water, $\rho_F/\rho_D \approx 0.1$. Depending on the studied geometry, the choice of Δt may be critical to stabilize the calculation. $\Delta t \sim 10^{-6}$ s in our work, and $t_0 = \sqrt{\rho_D h/D} = 8.17 \cdot 10^{-2}$ s for the disk of the Presas et al. (2015) test rig. Hence, the dimensionless time $\Delta\tau = \Delta t/t_0 \sim 10^{-5}$ grants enough precision so that the fluid equations time discretization scheme needs not be of high order. Moreover, the highest mesh displacement in one time step is less than a hundred times the smallest cell size.

We then initialize the model in the rotating disk reference frame by setting the domain angular velocity to Ω_D. The rotating parts in the stationary reference frame are therefore considered stationary in the rotating disk reference frame. Casing walls are defined as counter-rotating. Centrifugal and Coriolis forces are accounted for in the fluid. At first, performing a steady state computation with $w = 0$ imposed allows the flow to stabilize in the rotating domain. Then enabling the mesh vertical motion and applying a sine pulse to the modal force during the first steps induces movement. We then leave the system to oscillate freely.

During the main calculation, we apply the following procedure to each time step of the

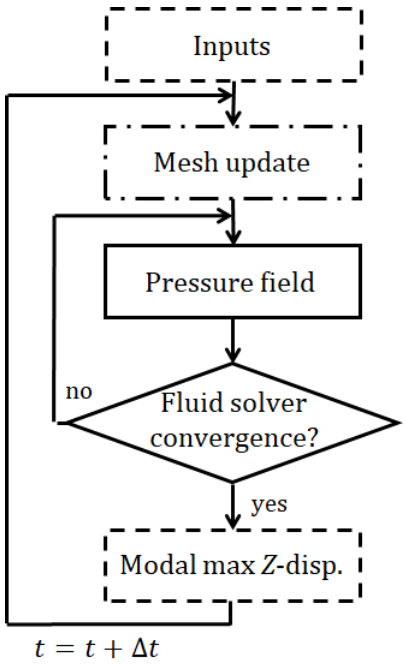

Figure 2.3 Working scheme for the numerical model. Continuous boxes symbolize steps solved within CFX, while dashed boxes represent steps solved with external user FORTRAN subroutines (Junction Box). The mesh update consists of solving Eq. (2.55). The maximum Z-displacement step is achieved with the resolution of Eqs. (2.56-2.57) using an adapted Runge-Kutta algorithm. Convergence is based on RMS criteria of conservative control volume fluid equation residuals.

simulation, as shown in Figure 2.3:

1. Pressure and velocity fields are computed in the fluid domain.
2. The pressure field is integrated on the disk, for each modeshape. The second order Eq. (2.19) is converted to a first order system of equations and then solved using the Runge-Kutta algorithm.
3. The new total mesh Z-displacement is calculated according to Eq. (2.55). The mesh is then updated.

A frequency analysis of the Z-displacement time signal provides the free oscillation frequencies of the system for the chosen mode.

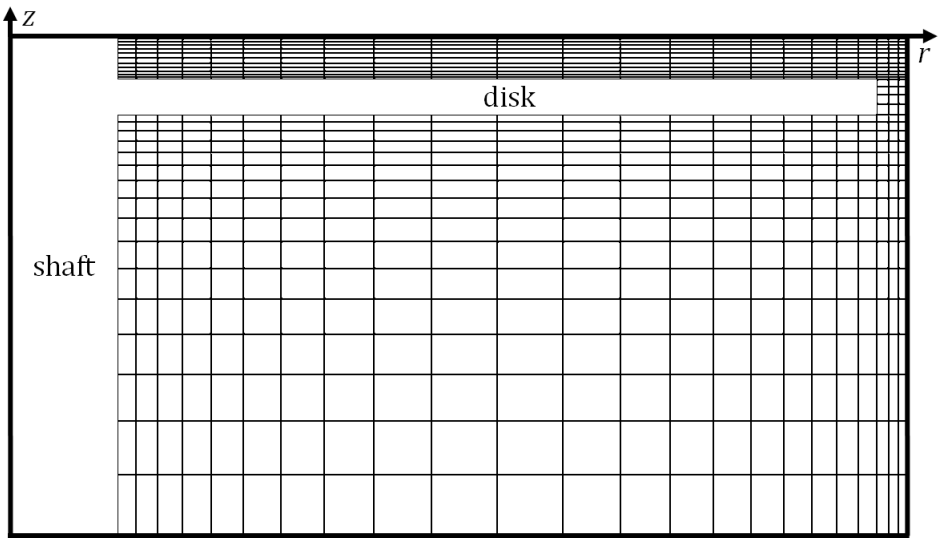

Figure 2.4 Fluid domain mesh of the Presas et al. (2015) experimental test rig in the (r, z) plan for the CFD model. Elements are cubic hexagonal, regularly spaced in the θ direction at intervals of $2°$. There are $10^5/n$ elements in this mesh, where n is the number of nodal diameters of the studied mode.

CHAPTER 3 RESULTS AND DISCUSSION

3.1 Analytical model results

In this section we analyse the modal analytical model for rotating and submerged disk natural frequency prediction, given by Eq. (2.52). Table 3.1 summarizes the parameters used to model the Presas et al. (2015) experimental test rig. Table 3.2 and Figure 3.1 present frequencies of this structure's natural frequencies for modes $n = 2, 3, 4$ nodal diameters and $s = 0$ nodal circles, assessed with Eq. (2.52). Their test rig uses a rotating disk in water, confined in a rigid casing, with small radial gap, which makes it particularly relevant with regards to our analytical model hypotheses. For a given mode, the natural frequencies of both co- and counter-rotating waves are identical when the disk is stationary. The split between ω_+ and ω_- then increases with the rotation speed, while the average value slightly decreases. Overall, Figure 3.1 illustrates that the model shows good accuracy with respect to Presas et al. (2015) experimental results.

Table 3.1 Parameter values for modeling the Presas et al. (2015) experimental test rig geometry. The disk is made of stainless steel; the fluid is water.

E	$200{\cdot}10^9$ Pa	ν	0.27
ρ_D	7680 kg/m^3	ρ_F	997 kg/m^3
a	0.2 m	b	0.025 m
H_{up}	0.01 m	H_{down}	0.097 m
h	0.008 m	K	0.45

Table 3.2 Natural frequencies of modes $n = \pm 2, 3, 4$, $s = 0$ obtained with the analytical model Eq. (2.52) and the Presas et al. (2015) experiments for different disk rotation speeds and the corresponding test rig geometry, and relative error ϵ. $f = |\omega|/2\pi$.

[Hz]	$n = 2$			$n = 3$			$n = 4$		
f_D	0	4	8	0	4	8	0	4	8
$f_{+,\text{exp}}$	127.1	120.1	117.4	321.2	317.8	309.1	642.2	619	607.9
$f_{+,\text{ana}}$	117.1	113.4	109.7	312.2	307.3	302.4	626.1	620.3	614.4
ϵ_+	7.9%	5.6%	6.6%	2.8%	3.3%	2.2%	2.5%	0.2%	1.1%
$f_{-,\text{exp}}$	127.1	126.9	132.3	321.2	328.2	330.0	642.2	630.6	633.7
$f_{-,\text{ana}}$	117.1	120.7	124.4	312.2	317.1	322.0	626.1	631.9	637.7
ϵ_-	7.9%	7.7%	4.9%	2.8%	4.9%	2.4%	2.5%	0.2%	0.6%

Our predictive analytical equation provides information on the two physical phenomena applying to disks rotating in a dense fluid. First, let us recall that $n > 0$ and $n < 0$ respectively

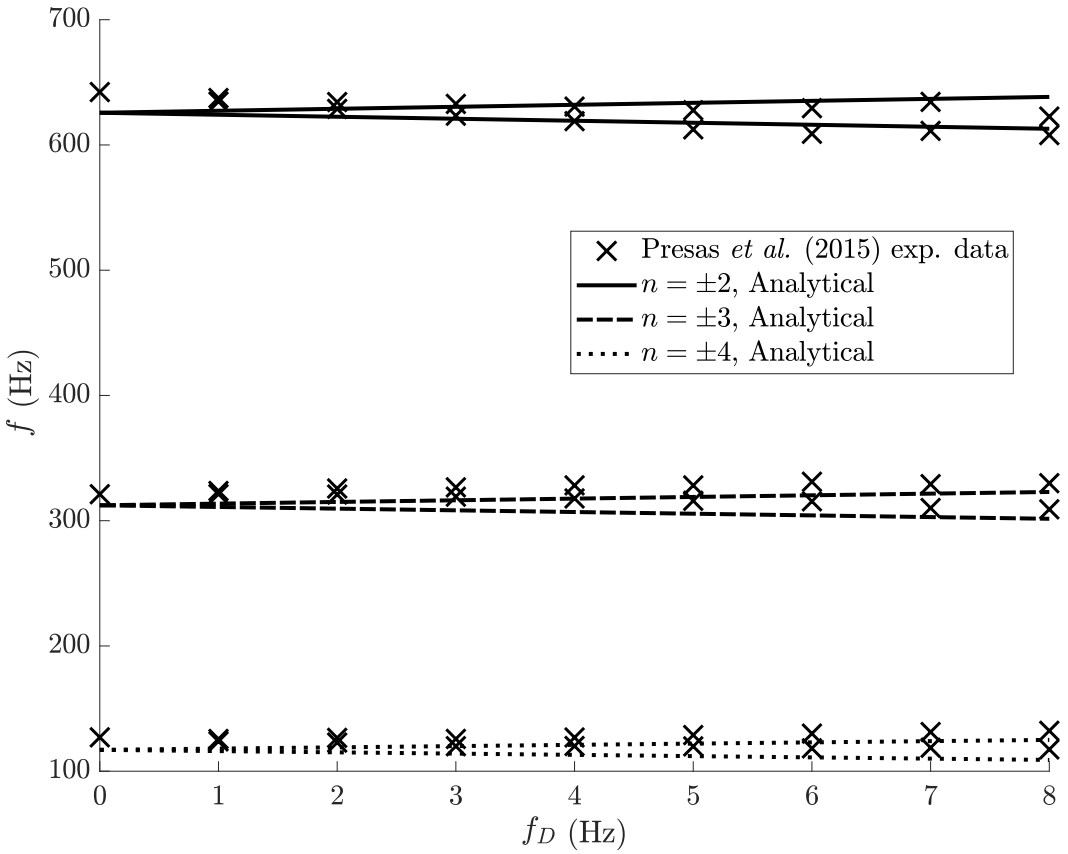

Figure 3.1 Comparison of the disk natural frequencies for modes $n = \pm\,2, 3, 4$, $s = 0$ and the Presas et al. (2015) test rig geometry; dotted data corresponds to their experimental results and lines where obtained with the analytical model detailed in this section. $f = |\omega|/2\pi$.

characterize co- and counter-rotating waves relative to the rotating disk. Therefore, the $-n\beta_0\Omega_{D/F}$ term in Eq. (2.52) is responsible for the mode split phenomenon: the natural frequency is increased by the disk rotation for counter-rotating waves, while it is decreased for co-rotating waves. The mode split magnitude is then given by

$$\omega_- - \omega_+ = \frac{2n\beta_0\Omega_{D/F}}{\beta_0 + 1}\,. \tag{3.1}$$

Secondly, the $-\beta_0(n\Omega_{D/F})^2$ term inside the square root of Eq. (2.52) is responsible for the frequency drift: it decreases the value of the frequency regardless of the propagation direction of the wave. Both of these terms are proportional to the relative rotation speed between the disk and the fluid multiplied by the number of nodal diameters. However, the frequency drift magnitude is smaller than the mode split magnitude for typical rotation speeds of high head runners.

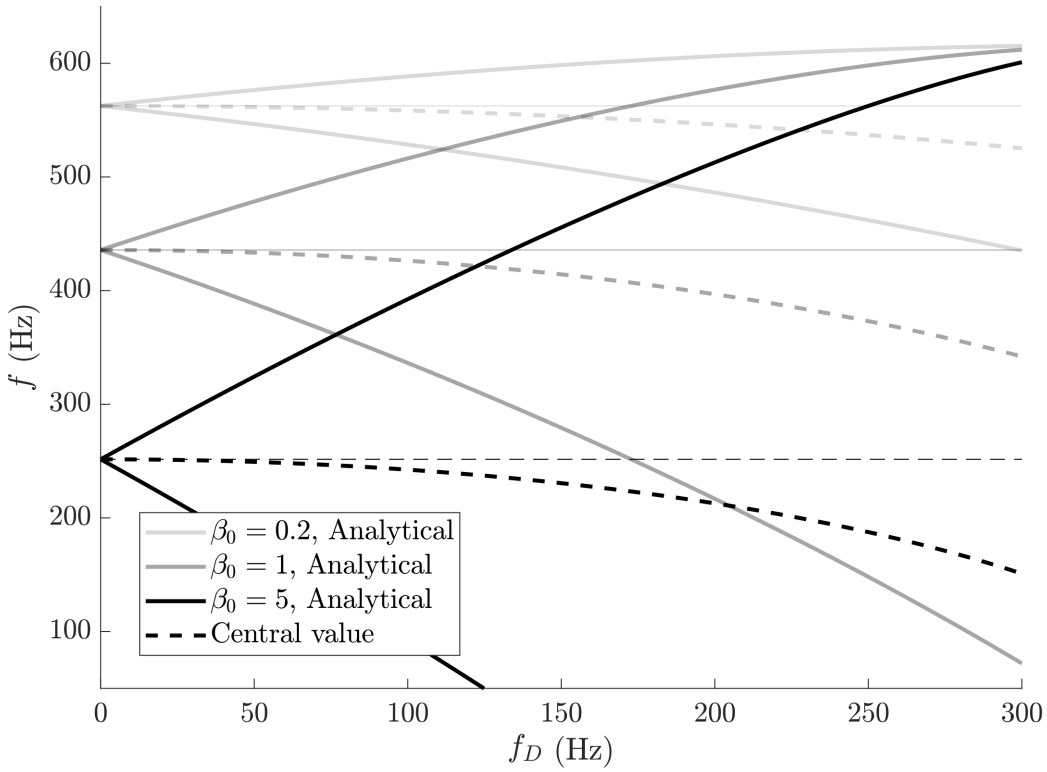

Figure 3.2 Disk analytical frequencies for mode $n = \pm 3$, $s = 0$ and a large range of disk rotating speeds. The system geometry is the same for all curves, but β_0 varies from 0.2 to 5. Black curves represent co- and counter-rotating mode frequencies, and the black dotted line shows the deviation from the $\Omega_D = 0$ natural frequency. This deviation is largest for $\beta_0 = 1$, while the mode split magnitude increases with β_0. Hydraulic turbines typically have $\Omega_D/2\pi \leq 10$ Hz. $f = |\omega|/2\pi$.

The influence of the considered mode and of both the disk and casing geometries on the structure natural frequencies is more difficult to interpret because of the complexity of the β_0 parameter. A parametric study shows that if the axial gap is large enough (typically $H_{up}, H_{down} \geq 0.2\,a$), β_0 is in the order of magnitude of the density ratio multiplied by the aspect ratio of the disk, while it tends towards infinity if this gap becomes null:

$$\beta_0\Big|_{H_{up},H_{down}\geq 0.2\,a} \propto \frac{\rho_F}{\rho_D}\frac{a}{h}\,, \qquad \lim_{H\to 0}\beta_0 = \infty\,. \tag{3.2}$$

Independently, it can be determined from Eq. (2.49) that β_0 increases with shorter axial gaps, and with larger and thinner disks. Additional numerical tests show that β_0 decreases with the number of nodal diameters and circles. Figure 3.2 presents the influence of β_0 on the natural frequencies predicted with our analytical model. The mode split magnitude increases with β_0 towards the asymptotic value of $2n\Omega_{D/F}$, which is also apparent from Eq. (3.1). The

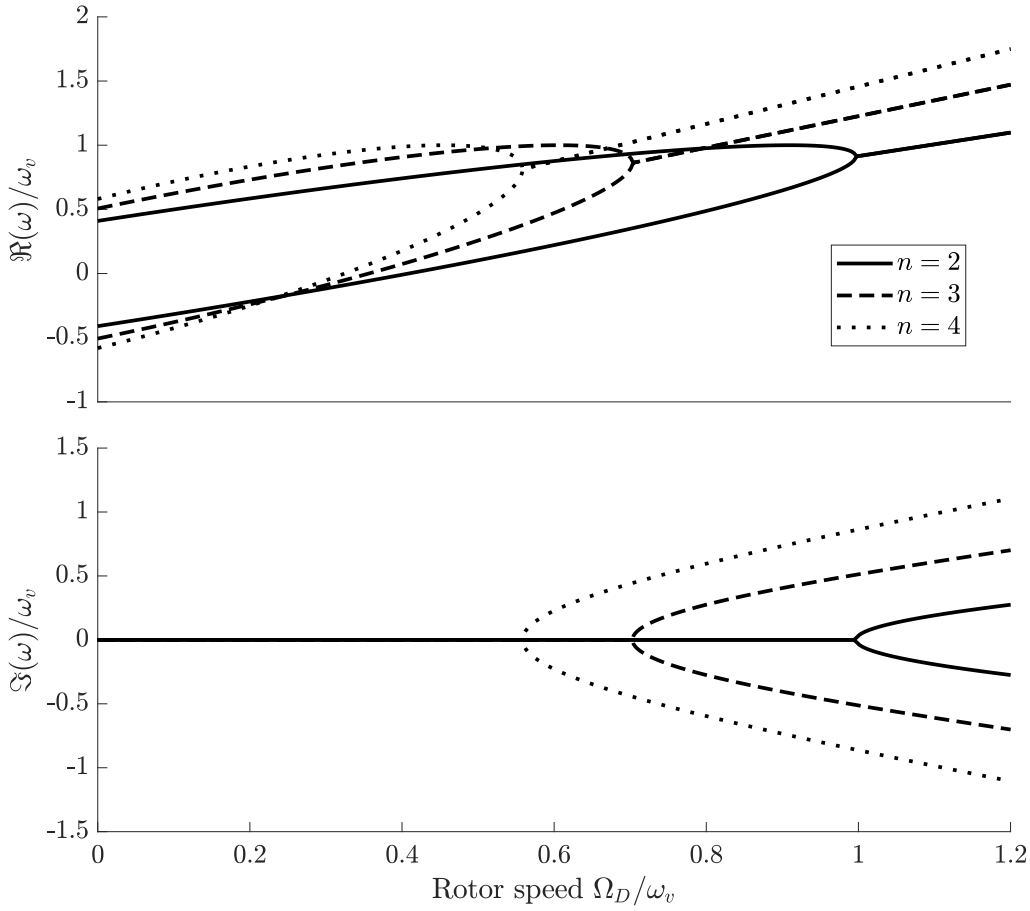

Figure 3.3 Real (top) and imaginary (bottom) parts of the Presas et al. (2015) disk natural frequencies for modes $n = 2, 3, 4$, $s = 0$. The two real natural frequencies of a single rotating mode eventually merge when the rotation speed reaches the critical speed. According to Eq. (3.3), the corresponding critical speeds are $\Omega_{C,n=2}/2\pi = 157$ Hz, $\Omega_{C,n=3}/2\pi = 238$ Hz and $\Omega_{C,n=4}/2\pi = 331$ Hz.

frequency drift magnitude presents a maximum for $\beta_0 = 1$. For typical turbine runner dimensions, rotation speeds ($\Omega_D/2\pi \leq 10$ Hz) and water density, the drift represents less than 1% of the predicted frequency. In conclusion, the frequency drift effect is negligible in terms of hydraulic turbine applications. This is not true for the frequency split, which needs to be predicted accurately.

We now consider both positive and negative frequencies (hence $n > 0$). Figure 3.3 presents the evolution of these natural frequencies with the rotation speed for several modes of the Presas et al. (2015) experimental test rig geometry. The frequencies become complex values for $\Omega_{D/F}$ above a critical value Ω_C. This happens when the term under the square root of Eq. (2.52) becomes negative, which triggers an unstable coupling between the disk movements and

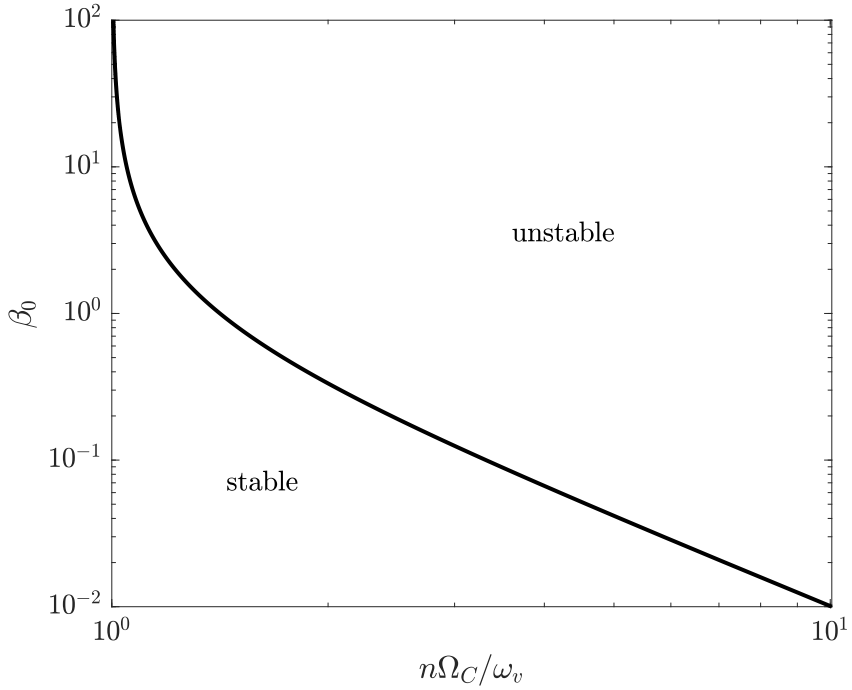

Figure 3.4 Log-log stability map for the Presas et al. (2015) experimental test rig geometry. For a given value of β_0, any rotation speed corresponding to a point on the right of the line is associated with coupled-mode flutter. The shape of the boundary is similar for any disk geometry, and given by Eq. (3.3).

the variation of pressure in the surrounding fluid (Kornecki, 1978; Kang and Raman, 2004). The associated instability is flutter (Huang and Mote, 1995; Kim et al., 2000), representing a classical Hopf bifurcation, characterized by pairs of natural frequencies with a non-zero imaginary part for $\Omega_{D/F} > \Omega_C$ (Païdoussis, 1998). The critical disk to fluid rotation speed Ω_C is given by

$$\frac{n\Omega_C}{\omega_v} = \sqrt{1 + \frac{1}{\beta_0}}\,. \tag{3.3}$$

Figure 3.4 shows the stability map for the non-dimensional critical speed as a function of β_0. Two asymptotic regimes emerge:

$$\lim_{\beta_0 \to 0} \Omega_C = \infty\,, \qquad \lim_{\beta_0 \to \infty} \Omega_C = \omega_v/n\,. \tag{3.4}$$

This second part in Eq. (3.4) shows that critical speeds are much above the hydraulic turbine applications range for any mode and typical geometries.

3.2 Numerical model results

In this section we validate the hypothesis made on the entrainment coefficient K, and we analyze the modal numerical model results for stationary or rotating disks in air or water. All geometrical and physical parameters remain as given in Table 3.1, and the radial gap is 7 mm long. According to Poncet et al. (2005), the average entrainment coefficient of the flow between a radially delimited rotating and stationary frame satisfies

$$K \approx 0.45 \text{ for } 10^6 < Re = \Omega_D a^2/\nu < 4.5 \cdot 10^6\,, \tag{3.5}$$

where Re is the Reynolds number and ν is the kinematic viscosity of the fluid. Figure 3.5 presents the fluid rotation speed relative to the disk in the top axial gap, computed with CFD. The fluid obeys the no-slip boundary condition and rotates with the disk on its surface ($\Omega_{D/F} = 0$ at $\hat{z} = 0$), it is stationary on the casing surface ($\Omega_{D/F} = \Omega_D$ at $\hat{z} = \hat{H}_{up}$), and it rotates at $\Omega_{D/F} \approx 0.55\,\Omega_D$ for $0.1 < \hat{z}/\hat{H}_{up} < 0.9$. This verifies that $K \approx 0.45$ for the tested geometry, and validates the hypothesis made in the analytical model development.

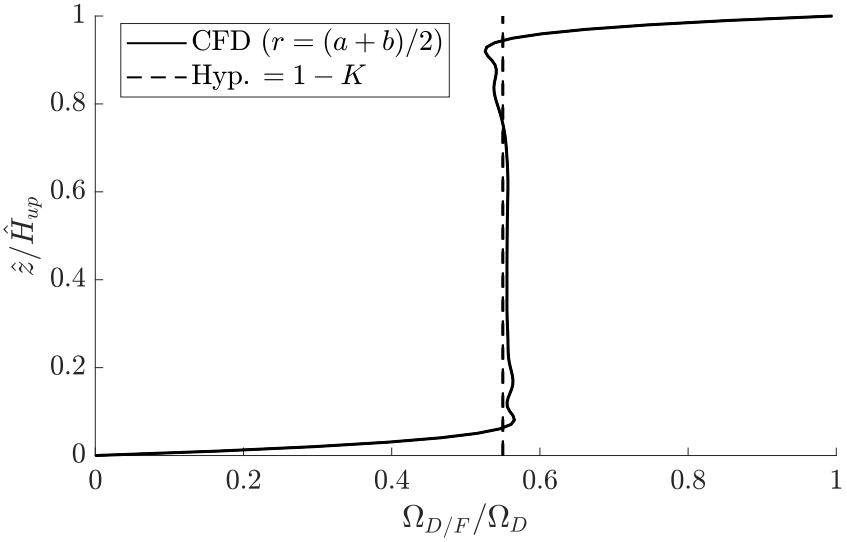

Figure 3.5 Rotation speed of the disk relative to the fluid in the axial gap above the disk at the middle radius $r = (a+b)/2$. Results were obtained with CFD for the Presas et al. (2015) experimental test rig geometry rotating at $\Omega_D/2\pi = 4$ Hz; $\hat{z} = 0$ corresponds to the rotor surface, while $\hat{z} = \hat{H}_{up}$ corresponds to the top part of the casing. The values agree with the theoretical expression of $\Omega_{D/F}/\Omega_D = 1 - K$ and $K = 0.45$ (dashed line).

Figure 3.6 presents the q_c and q_s signals from Eqs. (2.56-2.57) for a disk in air. We matched the disk geometry with the Presas et al. (2015) experimental test rig. The vertical displace-

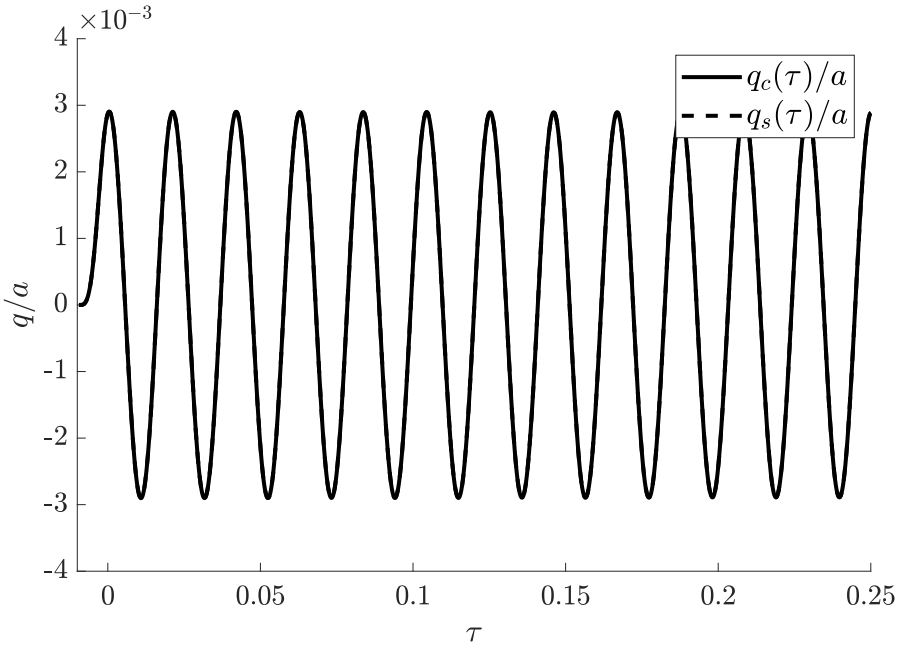

Figure 3.6 q_c/a and q_s/a as a function of the elapsed dimensionless time for mode $n = 3$, $s = 0$ and the Presas et al. (2015) geometry. The simulation begins with an initial sine pulse, followed by free oscillations of the standing disk in air. Both signals have identical frequencies and the fluid damping is negligible. Structural damping is not taken into account in the CFD analysis. Here $\omega/2\pi = 616.2$ Hz matches the structure natural frequency.

ment appears as periodic and harmonic, with angular frequency $\omega_+ = \omega_-$. With low density fluids such as air at 25°C, the influence of the fluid and of the disk rotation on the natural frequencies is negligible, as Eq. (3.2) implies $\beta_0 \sim 10^{-3} \ll 1$ for geometries of interest. Hence, the identical frequencies for both signals. The fluid damping is also very low.

Figure 3.7 presents the q_c and q_s signals for the same stationary disk, in water. With no rotation, we still have $\omega_+ = \omega_-$. However, the signal amplitude now decreases with time. Computed frequencies for several modes are compared, and agree, with the Presas et al. (2015) experimental results and with Eq. (2.52) in Table 3.3. The presence of the radial gap in the CFD model is thought to be largely responsible for the small differences between analytical and numerical results. With high density fluids such as water, the fluid influence is no longer negligible, as Eq. (3.2) implies $\beta_0 \sim 1$ for geometries of interest. For non-rotating disks, the two main effects of the fluid are the decrease of structural natural frequencies and the damping of the displacement amplitude.

Figure 3.8 presents the q_c and q_s signals for the same disk, rotating in water. The signal is still damped because of the dense fluid. Adding the rotation of the disk in dense fluid triggers

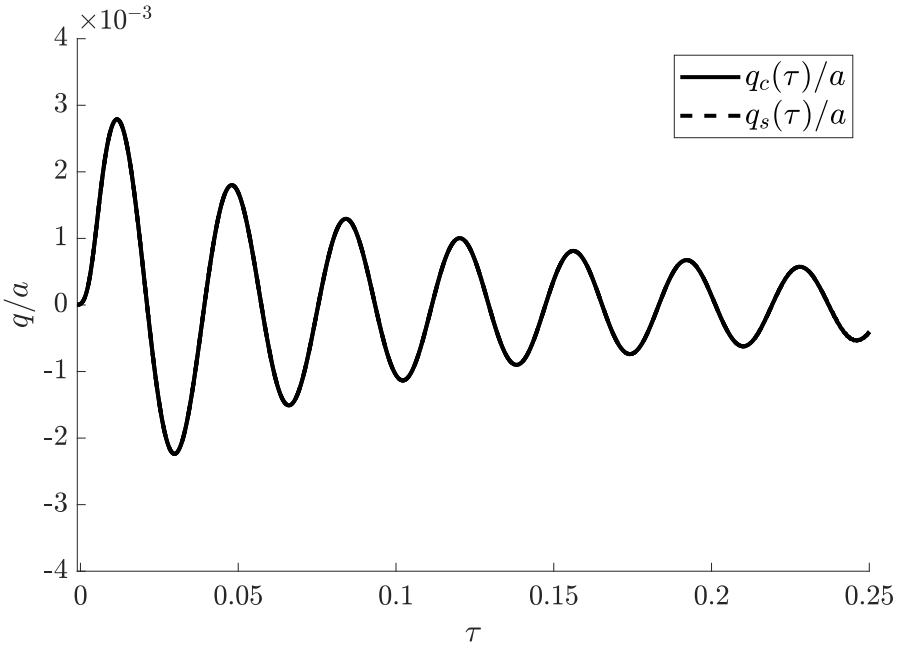

Figure 3.7 q_c/a and q_s/a as a function of the elapsed dimensionless time for mode $n = 3$, $s = 0$ and the Presas et al. (2015) geometry. The simulation begins with an initial sine pulse, followed by free oscillations of the standing disk in water. Both signals have identical frequencies and their amplitude is damped by the dense fluid. Here $\omega/2\pi = 340.3$ Hz agrees with both the analytical model and the experimental data.

the mode split phenomenon, because of the fluid's different interaction with the co- and counter-rotating waves, as shown in Eq. (2.52). Both signals now show a beat envelope, due to the presence of two close frequencies: ω_+ and ω_-. The high frequency can be interpreted as the natural angular frequencies average $(\omega_- + \omega_+)/2$, which is usually close to the non-rotating disk natural angular frequency in water. The beat frequency corresponds to half the mode split magnitude given by Eq. (3.1). Table 3.4 compares mode split magnitudes obtained with both analytical and numerical methods for several modes; the agreeing results show how well the physics is captured. The physical interpretation of this split is that the previously stationary mode now rotates slowly at half of the mode split angular frequency magnitude $(\omega_- - \omega_+)/2$. The combination of both measured frequencies $(\omega_- + \omega_+)/2$ and $(\omega_- - \omega_+)/2$ allows determining the actual natural angular frequencies of the rotating disk in dense fluid:

$$\omega_+ = \left(\frac{\omega_- + \omega_+}{2}\right) - \left(\frac{\omega_- - \omega_+}{2}\right), \tag{3.6}$$

$$\omega_- = \left(\frac{\omega_- + \omega_+}{2}\right) + \left(\frac{\omega_- - \omega_+}{2}\right). \tag{3.7}$$

Table 3.3 Natural frequencies of modes $n = 2, 3, 4$, $s = 0$ obtained with the analytical model Eq. (2.52), the numerical model Eq. (2.19), and experiments from Presas et al. (2015) for the stationary disk in water, and relative error ϵ. $f = |\omega|/2\pi$.

[Hz]	$n = 2$	$n = 3$	$n = 4$
f_{exp}	127.1	321.2	642.2
f_{ana}	117.1	312.2	626.1
$\epsilon_{\text{ana}-\text{exp}}$	7.9%	2.8%	2.5%
f_{num}	130.1	340.3	641.2
$\epsilon_{\text{num}-\text{exp}}$	2.4%	5.9%	0.2%

Table 3.4 Split magnitude of modes $n = \pm 2, 3, 4$, $s = 0$ obtained with the analytical model Eq. (3.1) and the numerical model Eqs. (2.56-2.57) for the Presas et al. (2015) rotating disk at $\Omega_D/2\pi = 40$ Hz in water, and relative error ϵ. $f = |\omega|/2\pi$.

[Hz]	$n = 2$	$n = 3$	$n = 4$
$\lvert f_- - f_+\rvert_{,\text{ana}}$	73.2	98.1	116.6
$\lvert f_- - f_+\rvert_{,\text{num}}$	73.8	95.9	115.2
$\epsilon_{\text{ana}-\text{num}}$	0.8%	2.2%	1.2%

After a certain simulated time that depends on geometrical and numerical parameters, interfering high frequency oscillations appear and prevent the observation of the beating oscillation, and therefore of the split. However, they can been easily avoided without modifying the disk natural frequencies by increasing the fluid compressibility, as discussed in Appendix E.

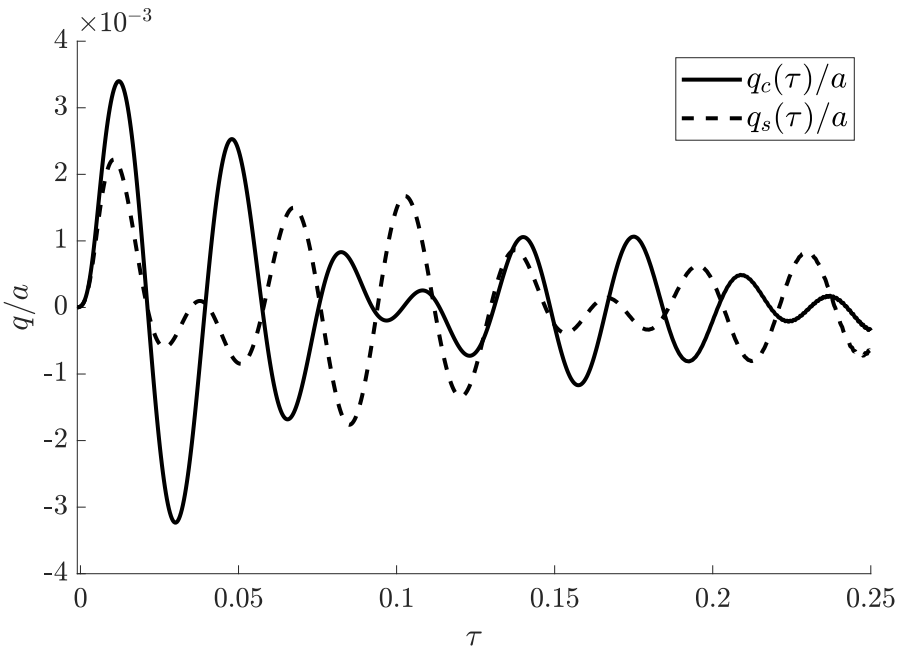

Figure 3.8 q_c/a and q_s/a as a function of the elapsed dimensionless time for mode $n = 3$, $s = 0$ and the Presas et al. (2015) geometry. The simulation begins with an initial sine pulse, followed by free oscillations of the rotating disk in water ($\Omega_D/2\pi = 4$ Hz). Both signals have close but different frequencies, which results in a beating oscillation, characteristic of free vibration under mode split. Here $|\omega_- - \omega_+|/2\pi = 95.9$ Hz agrees with the analytical model.

CHAPTER 4 CONCLUSION

4.1 Summary of Works

The analytical modal approach applied to disks gives information on the potential flow in the fluid domain above and below the plate. This further results in the determination of the AVMI factor β_0, characterizing the fluid effect on the structural vibrations. Eventually, we determined an analytical expression for co- and counter-rotating wave angular frequencies:

$$\omega = \frac{\sqrt{(\beta_0+1)\omega_v^2 - \beta_0(n\Omega_{D/F})^2} - n\beta_0\Omega_{D/F}}{\beta_0+1}\,.$$

This model uses two assumptions, namely that potential flow is a good approximation and that the empirical value for the entrainment coefficient to determine the effective fluid rotation $\Omega_{D/F}$ is correct. Accepting these assumptions, the model is truly predictive, solvable in only a few seconds, and takes into account the geometry (including axial gaps, but not the radial gap), the fluid and structure characteristics, and the disk rotation. Both the frequency split and drift that result from the disk motion in dense fluid are well captured. The split amplitude asymptotic behavior is given by

$$\lim_{\beta_0\to\infty} |\omega_- - \omega_+| = 2n\Omega_{D/F}\,.$$

The modal approach applied to an arbitrary number of disk modes provides a 1DOF representation of single propagating waves. We extended this model to a 2DOF representation of companion mode pairs, namely co- and counter-rotating waves of single modes. The temporal unknowns q_c and q_s verify equations given by the Galerkin method resolution. We simulated freely vibrating rotating disks in dense fluid using Ansys CFX fluid solver coupled to the discretized equations with a Runge-Kutta method, while imposing specific modeshapes to the structure. Fluid damping and mode split are well captured. Mode split translates into a stationary mode when observed from the reference frame rotating at $(\omega_- - \omega_+)/2$. Both analytical and numerical approaches agree with experimental data from Presas et al. (2015), and provide physical interpretation of mode split.

Our work improves knowledge of the dynamical characteristics of high head hydraulic turbines by providing means to assess the variation of rotor natural frequencies with rotation speed and added mass of the surrounding water, which facilitates potential resonance identification within a shorter time. Our parametric and stability studies additionally show that

frequency drift and flutter instability do not occur within hydraulic turbine operation range. Both models developed in this study provide fast tools for preliminary studies on high head hydraulic turbine vibrations, and ways to explore parameters influencing mode split.

4.2 Limitations

Although extremely fast, the modal analytical approach limits the frequency prediction to single independent modes for disk geometries without radial gaps. This may not be realistic for some vibrating systems, and restrains its use for direct hydraulic turbine frequency prediction. However, it remains an efficient tool for understanding the physics of the mode split.

The analytical CFD model provides a fast natural frequency prediction model with limited predictive value. It proves efficient for exploring the physics of hydraulic turbine related resonance phenomena, and the influence of involved parameters. The observed parasitic high frequency vibrations that may arise limit the mode split observation at low rotation speeds.

4.3 Future Research

Although we studied the rotating disk alone, Valentín et al. (2015) showed that the casing flexibility may induce coupling with the rotating disk, resulting in the modification of its natural frequencies, especially if the gaps are small. Typically, in hydraulic turbines, this issue arises when the top part of the runner vibrates with the top casing surface (Weder et al., 2019). This makes rotor-stator coupling especially relevant for future work on the matter; possibly by adapting our numerical model. Eliminating the high frequency oscillations on the latter could be achieved by transferring the structural solver from the Fortran routines to ANSYS APDL, through System Coupling; allowing the solver to perform convergence checks on both fluid and structure equations.

REFERENCES

G. Adams, "Critical speeds for a flexible spinning disk", *International Journal of Mechanical Sciences*, vol. 29, no. 8, pp. 525–531, 1987.

T. Ahn and C. Mote, "Mode identification of a rotating disk", *Experimental mechanics*, vol. 38, no. 4, pp. 250–254, 1998.

M. Amabili and M. Kwak, "Free vibrations of circular plates coupled with liquids: revising the lamb problem", *Journal of fluids and structures*, vol. 10, no. 7, pp. 743–761, 1996.

M. Amabili, G. Frosali, and M. Kwak, "Free vibrations of annular plates coupled with fluids", *Journal of sound and vibration*, vol. 191, no. 5, pp. 825–846, 1996.

D. Biner, "Hydrodynamic damping and added stiffness prediction on a rotor-stator disk assembly in water using a modal approach", Ph. D. thesis, Haute École Spécialisée de Suisse occidentale, 2017.

M. Bossio *et al.*, "Numerical study on the influence of acoustic natural frequencies on the dynamic behaviour of submerged and confined disk-like structures", *Journal of Fluids and Structures*, vol. 73, pp. 53–69, 2017.

A. Coutu *et al.*, "Dynamic assessment of hydraulic turbines", *Proceedings of HydroVision*, pp. 16–20, 2004.

——, "Experience with rotor-stator interactions in high head francis runner", in *24th IAHR Symposium on Hydraulic Machinery and Systems, Foz do Iguaçu, Brazil, Oct*, 2008, pp. 27–31.

F. Dompierre and M. Sabourin, "Determination of turbine runner dynamic behaviour under operating condition by a two-way staggered fluid-structureinteraction method", in *IOP Conference Series: Earth and Environmental Science*, vol. 12, no. 1. IOP Publishing, 2010, p. 012085.

P. Dörfler, M. Sick, and A. Coutu, *Flow-induced pulsation and vibration in hydroelectric machinery: engineer's guidebook for planning, design and troubleshooting.* Springer Science & Business Media, 2012.

E. Egusquiza *et al.*, "Analysis of the dynamic response of pump-turbine impellers. influence of the rotor", *Mechanical Systems and Signal Processing*, vol. 68, pp. 330–341, 2016.

X. Escaler and O. De La Torre, "Axisymmetric vibrations of a circular chladni plate in air and fully submerged in water", *Journal of Fluids and Structures*, vol. 82, pp. 432–445, 2018.

J. Hengstler, "Influence of the fluid-structure interaction on the vibrations of structures", Ph. D. thesis, ETH Zurich, 2013.

F. Huang and C. Mote, "On the instability mechanisms of a disk rotating close to a rigid surface", *Journal of Applied Mechanics*, vol. 62, no. 3, pp. 764–771, 1995.

B. Hübner, W. Weber, and U. Seidel, "The role of fluid-structure interaction for safety and life time prediction in hydraulic machinery", in *IOP Conference Series: Earth and Environmental Science*, vol. 49, no. 7. IOP Publishing, 2016, p. 072007.

H.-J. Huth, "Fatigue design of hydraulic turbine runners", Ph. D. thesis, Fakultet for ingeniørvitenskap og teknologi, 2005.

N. Kang and A. Raman, "Vibrations and stability of a flexible disk rotating in a gas-filled enclosure—part 1: Theoretical study", *Journal of sound and vibration*, vol. 296, no. 4-5, pp. 651–675, 2006.

——, "Vibrations and stability of a flexible disk rotating in a gas-filled enclosure—part 2: Experimental study", *Journal of Sound and Vibration*, vol. 296, no. 4-5, pp. 676–689, 2006.

——, "Aeroelastic flutter mechanisms of a flexible disk rotating in an enclosed compressible fluid", *Journal of applied mechanics*, vol. 71, no. 1, pp. 120–130, 2004.

B. Kim, A. Raman, and C. Mote Jr, "Prediction of aeroelastic flutter in a hard disk drive", *Journal of sound and vibration*, vol. 238, no. 2, pp. 309–325, 2000.

A. Kornecki, "Aeroelastic and hydroelastic instabilities of infinitely long plates. i", *Solid Mechanics Archives*, vol. 3, pp. 381–440, 1978.

Y. Kubota and H. Ohashi, "A study on the natural frequencies of hydraulic pumps", in *Proceedings of the 1st ASME Joint International Conference on Nuclear Engineering, Tokyo, Japan*, 1991, pp. 4–7.

M. Kwak and K. Kim, "Axisymmetric vibration of circular plates in contact with fluid", *Journal of Sound and Vibration*, vol. 146, no. 3, pp. 381–389, 1991.

A. Leissa, "Vibration of plates", OHIO STATE UNIV COLUMBUS, Tech. rep., 1969.

Q. Liang *et al.*, "Numerical simulation of fluid added mass effect on a francis turbine runner", *Computers & Fluids*, vol. 36, no. 6, pp. 1106–1118, 2007.

X. Liu, Y. Luo, and Z. Wang, "A review on fatigue damage mechanism in hydro turbines", *Renewable and Sustainable Energy Reviews*, vol. 54, pp. 1–14, 2016.

C. Monette *et al.*, "Hydro-dynamic damping theory in flowing water", in *IOP Conference Series: Earth and Environmental Science*, vol. 22, no. 3. IOP Publishing, 2014, p. 032044.

B. Nennemann, C. Monette, and J. Chamberland-Lauzon, "Hydrodynamic damping and stiffness prediction in francis turbine runners using cfd", in *IOP Conference Series: Earth and Environmental Science*, vol. 49, no. 7. IOP Publishing, 2016, p. 072006.

P. Østby *et al.*, "Experimental investigation on the effect off near walls on the eigen frequency of a low specific speed francis runner", *Mechanical Systems and Signal Processing*, vol. 118, pp. 757–766, 2019.

M. P. Païdoussis, *Fluid-structure interactions: slender structures and axial flow*. Academic press, 1998, vol. 1.

S. Poncet, M.-P. Chauve, and R. Schiestel, "Batchelor versus stewartson flow structures in a rotor-stator cavity with throughflow", *Physics of fluids*, vol. 17, no. 7, p. 075110, 2005.

A. Presas *et al.*, "Experimental analysis of the dynamic behavior of a rotating disk submerged in water", in *IOP Conference Series: Earth and Environmental Science*, vol. 22, no. 3. IOP Publishing, 2014, p. 032043.

——, "Influence of the rotation on the natural frequencies of a submerged-confined disk in water", *Journal of Sound and Vibration*, vol. 337, pp. 161–180, 2015.

——, "Dynamic response of a rotating disk submerged and confined. influence of the axial gap", *Journal of Fluids and Structures*, vol. 62, pp. 332–349, 2016.

——, “Fatigue life estimation of francis turbines based on experimental strain measurements: Review of the actual data and future trends”, *Renewable and Sustainable Energy Reviews*, vol. 102, pp. 96–110, 2019.

A. Renshaw, “Critical speed for floppy disks”, *Journal of Applied Mechanics*, vol. 65, no. 1, pp. 116–120, 1998.

A. Renshaw, C. D’Angelo III, and C. Mote Jr, “Aerodynamically excited vibration of a rotating disk”, *Journal of Sound and Vibration*, vol. 177, no. 5, pp. 577–590, 1994.

A. Soltani Dehkharqani, M. Cervantes, and J.-O. Aidanpää, “Numerical analysis of fluid-added parameters for the torsional vibration of a kaplan turbine model runner”, *Advances in Mechanical Engineering*, vol. 9, no. 10, p. 1687814017732893, 2017.

A. Soltani Dehkharqani *et al.*, “Fluid added polar inertia and damping for the torsional vibration of a kaplan turbine model runner considering multiple perturbations”, in *IOP Conference Series: Earth and Environmental Science*, vol. 240, no. 6. IOP Publishing, 2019, p. 062007.

R. Southwell, “On the free transverse vibrations of a uniform circular disc clamped at its centre; and on the effects of rotation”, *Proc. R. Soc. Lond. A*, vol. 101, no. 709, pp. 133–153, 1922.

M. Specker, “Simulation of the structure-structure coupling by liquids using comsol”, Ph. D. thesis, ETH Zurich, 2016.

C. Trivedi and M. Cervantes, “Fluid-structure interactions in francis turbines: A perspective review”, *Renewable and Sustainable Energy Reviews*, vol. 68, pp. 87–101, 2017.

A. Trondal Svendsen and A. Michaelsen, “Aeroelastic response of high-rise buildings”, Ph. D. thesis, Aalborg Universitet, 2008.

D. Valentín *et al.*, “Experimental study on the added mass and damping of a disk submerged in a partially fluid-filled tank with small radial confinement”, *Journal of Fluids and Structures*, vol. 50, pp. 1–17, 2014.

——, “Influence of non-rigid surfaces on the dynamic response of a submerged and confined disk”, in *Cavitation and dynamic problems: 6 th IAHR meeting of the Working Group,*

IAHRWG 2015: Ljubljana, Slovenia, September 9-11, 2015: Proceedings, 2015, pp. 251–258.

——, "On the capability of structural–acoustical fluid–structure interaction simulations to predict natural frequencies of rotating disklike structures submerged in a heavy fluid", *Journal of Vibration and Acoustics*, vol. 138, no. 3, p. 034502, 2016.

S. Vogel and D. Skinner, "Natural frequencies of transversely vibrating uniform annular plates", *Journal of Applied Mechanics*, vol. 32, no. 4, pp. 926–931, 1965.

E. Walton and C. Tan, "Forced response of a centrifugal compressor stage due to the impeller–diffuser interaction", *Journal of Turbomachinery*, vol. 138, no. 9, p. 091004, 2016.

W. Weber and U. Seidel, "Analysis of natural frequencies of disc-like structures in water environment by coupled fluid-structure-interaction simulation 6th iahr international meeting of the workgroup on cavitation and dynamic problems in hydraulic machinery and systems (ljubljana,)", in *6th IAHR International Meeting of the Workgroup on Cavitation and Dynamic Problems in Hydraulic Machinery and Systems.(Cited on page 41.)*, 2015.

M. Weder *et al.*, "Structure-structure coupling by liquids: Vibration measurements on a rotating disk with self-tracking ldv", in *AIP Conference Proceedings*, vol. 1740, no. 1. AIP Publishing, 2016, p. 080002.

——, "Experimental modal analysis of disk-like rotor–stator system coupled by viscous liquid", *Journal of Fluids and Structures*, vol. 88, pp. 198–215, 2019.

K. Wong *et al.*, "Numerical stability of partitioned approach in fluid-structure interaction for a deformable thin-walled vessel", *Computational and mathematical methods in medicine*, vol. 2013, 2013.

APPENDIX A MATLAB CODE: NUMERICAL RESOLUTION OF THE MODAL APPROACH FOR DISKS

This code computes the split natural frequencies (in rad/s or Hz), modeshapes and NAVMI factor of free-clamped rings rotating in a fluid for a given number of nodal diameters and circles; the geometry is customizable. It also allows for simple Dirac forced response analysis and flutter instability domain determination. This code refers to equations from Leissa (1969) and Amabili et al. (1996). The execution time for a single frequency pair is about one second.

```
%% Parameters
%~Output unit (Hz or rad/s)
hertz = true; % 'false' for rad/s, 'true' for Hz // use rad/s for input
%~Material
    E = 200*10^9; % Young's modulus (Pa)
    nu = 0.27; % Poisson's ratio
    rhoD = 7680; % mass density of the solid (kg/m3)
%~Fluid
    rhoF = 0.997; % mass density of the fluid (kg/m3)
    K = 0.45; % entrainment coefficient
%~Geometry
    a = 0.2; % outer radius of the plate (m)
    b = 0.05; % inner radius of the plate (m)
    % always works for b/a <= 0.125, otherwise may need correction
    h = 0.008; % plate thickness (m)
    Hup = 0.01; % top axial gap (m)
    Hdown = 0.097; % bottom axial gap (m)
Df = E*h^3/12/(1-nu^2); % flexural rigidity (N.m)
%~Rotation speed
OmegaD = 25.1327; % disk angular velocity (rad/s)
if hertz == true
    OmegaD = OmegaD/2/pi;   % (Hz)
end
%~Mode
n = 3; % diametrical mode
s = 0; % circular mode
```

```
%% k calculation
syms k      % k^4 = rhoD*h*omega^2/Df
if (n==0 || n==1)
    initk = (3.75*s+1.6)/a; % corrected guess value
else
    initk = (3.35*s+1.15*n)/a; % corrected guess value
end

A1 = besselj(n,k*b); % coefficients A1...D4 found with Maple symbolic
B1 = bessely(n,k*b); %   resolution of the boundary conditions, namely:
C1 = besseli(n,k*b); %   W(b)=dW(b)/dr=0 (clamped inside)
D1 = besselk(n,k*b); %   Vr(a)=Mr(a)=0 (free outside)
A2 = besselj(n+1,k*b)*k*b-n*besselj(n,k*b);
B2 = bessely(n+1,k*b)*k*b-n*bessely(n,k*b);
C2 = -besseli(n+1,k*b)*k*b-n*besseli(n,k*b);
D2 = besselk(n+1,k*b)*k*b-n*besselk(n,k*b);
A3 = k^3*a^3*besselj(n+1,k*a)-n^2*nu*besselj(n,k*a)...
    -n^2*nu*besselj(n+1,k*a)*k*a+n^2*besselj(n,k*a)-n^3*besselj(n,k*a)...
    +k*a*besselj(n+1,k*a)*n^2-n*k^2*a^2*besselj(n,k*a)...
    +n^3*nu*besselj(n,k*a);
B3 = k^3*a^3*bessely(n+1,k*a)-n^2*nu*bessely(n,k*a)...
    -n^2*nu*bessely(n+1,k*a)*k*a+n^2*bessely(n,k*a)-n^3*bessely(n,k*a)...
    +k*a*bessely(n+1,k*a)*n^2-n*k^2*a^2*bessely(n,k*a)...
    +n^3*nu*bessely(n,k*a);
C3 = k^3*a^3*besseli(n+1,k*a)-n^2*nu*besseli(n,k*a)...
    +n^2*nu*besseli(n+1,k*a)*k*a+n^2*besseli(n,k*a)-n^3*besseli(n,k*a)...
    -k*a*besseli(n+1,k*a)*n^2+n*k^2*a^2*besseli(n,k*a)...
    +n^3*nu*besseli(n,k*a);
D3 = -k^3*a^3*besselk(n+1,k*a)-n^2*nu*besselk(n,k*a)...
    -n^2*nu*besselk(n+1,k*a)*k*a+n^2*besselk(n,k*a)-n^3*besselk(n,k*a)...
    +k*a*besselk(n+1,k*a)*n^2+n*k^2*a^2*besselk(n,k*a)...
    +n^3*nu*besselk(n,k*a);
A4 = -nu*besselj(n+1,k*a)*k*a-k^2*a^2*besselj(n,k*a)...
    +besselj(n+1,k*a)*k*a+nu*n*besselj(n,k*a)-n^2*nu*besselj(n,k*a)...
    +n^2*besselj(n,k*a)-n*besselj(n,k*a);
```

```
B4 = -nu*bessely(n+1,k*a)*k*a-k^2*a^2*bessely(n,k*a)...
    +bessely(n+1,k*a)*k*a+nu*n*bessely(n,k*a)-n^2*nu*bessely(n,k*a)...
    +n^2*bessely(n,k*a)-n*bessely(n,k*a);
C4 = nu*besseli(n+1,k*a)*k*a+k^2*a^2*besseli(n,k*a)...
    -besseli(n+1,k*a)*k*a+nu*n*besseli(n,k*a)-n^2*nu*besseli(n,k*a)...
    +n^2*besseli(n,k*a)-n*besseli(n,k*a);
D4 = -nu*besselk(n+1,k*a)*k*a+k^2*a^2*besselk(n,k*a)...
    +besselk(n+1,k*a)*k*a+nu*n*besselk(n,k*a)-n^2*nu*besselk(n,k*a)...
    +n^2*besselk(n,k*a)-n*besselk(n,k*a);
M = [A1 B1 C1 D1   % M . {An Bn Cn Dn}' = 0
     A2 B2 C2 D2   % k verifies det(M)=0
     A3 B3 C3 D3
     A4 B4 C4 D4];
k1 = vpasolve(det(M)==0,k,initk);
k1 = double(subs(k1))
lambda = k1*a;      % frequency parameter

%% Omega calculation
Ms = rhoD*h*pi*(a^2-b^2);       % structural modal mass (kg)
Ks = Df*k1^4*pi*(a^2-b^2);      % structural modal stiffness (N/m)
omegaA = sqrt(Ks/Ms)            % central frequency in vacuum (rad/s)
if hertz == true
    omegaA = omegaA/2/pi % (Hz)
end

%% Modeshape
syms BB CC DD % W = A*Jn+B*Yn+C*In+D*Kn
A = 1; % arbitrary choice to close the system of equations
[B,C,D] = vpasolve(subs(M(1:3,:),k,k1)*[1 BB CC DD]'==[0 0 0]',[BB,CC,DD]);
B = double(subs(B));    % M . {A B C D}' = 0
C = double(subs(C));
D = double(subs(D));

%% Displacement W
[r,theta] = meshgrid(b:(a-b)/50:a,0:pi/24:2*pi);
W = (A*besselj(n,k1.*r)+B*bessely(n,k1.*r)+C*besseli(n,k1.*r)...
```

```
    +D*besselk(n,k1.*r)).*cos(n.*theta); % displacement
figure(1);
surf(r.*cos(theta), r.*sin(theta), W); % modeshape

%% Added mass M
syms eta rho    % rho = r/a
HA = @(eta) 1./(lambda^2-eta.^2).*(lambda.*besselj(n,eta).*besselj(n+1,...
    lambda)-eta.*besselj(n+1,eta).*besselj(n,lambda))-b/a./(lambda^2 ...
    -eta.^2).*(lambda.*besselj(n,b/a.*eta).*besselj(n+1,b/a*lambda)...
    -eta.*besselj(n+1,b/a.*eta).*besselj(n,b/a*lambda));
HB = @(eta) 1./(lambda^2-eta.^2).*(lambda.*besselj(n,eta).*bessely(n+1,...
    lambda)-eta.*besselj(n+1,eta).*bessely(n,lambda))-b/a./(lambda^2 ...
    -eta.^2).*(lambda.*besselj(n,b/a.*eta).*bessely(n+1,b/a*lambda)...
    -eta.*besselj(n+1,b/a.*eta).*bessely(n,b/a*lambda));
HC = @(eta) 1./(lambda^2+eta.^2).*(lambda.*besselj(n,eta).*besseli(n+1,...
    lambda)+eta.*besselj(n+1,eta).*besseli(n,lambda))-b/a./(lambda^2 ...
    +eta.^2).*(lambda.*besselj(n,b/a.*eta).*besseli(n+1,b/a*lambda)...
    +eta.*besselj(n+1,b/a.*eta).*besseli(n,b/a*lambda));
HD = @(eta) 1./(lambda^2+eta.^2).*(-lambda.*besselj(n,eta).*besselk(n+1,...
    lambda)+eta.*besselj(n+1,eta).*besselk(n,lambda))-b/a./(lambda^2 ...
    +eta.^2).*(-lambda.*besselj(n,b/a.*eta).*besselk(n+1,b/a*lambda)...
    +eta.*besselj(n+1,b/a.*eta).*besselk(n,b/a*lambda));
H = @(eta) A.*HA(eta)+B.*HB(eta)+C.*HC(eta)+D.*HD(eta);
    % obtained from resolution with Hankel transform
W = @(rho) (A.*besselj(n,lambda.*rho)+B.*bessely(n,lambda.*rho)...
    +C.*besseli(n,lambda.*rho)+D.*besselk(n,lambda.*rho));
fun = @(eta,rho) rhoF*a*H(eta).*besselj(n,eta.*rho).*W(rho);
M = integral2(fun,0,Inf,b/a,1,'AbsTol',1e-2)     % added mass (kg)
% expression is obtained through the calculation of the work rate and
% the integration on the top and bottom surfaces of the disk

%% NAVMI factor
syms eta rho    % rho = r/a
if n == 0       % integral of cos(n*theta)^2 over 0..2*pi
    psi = 2*pi;
else
```

```
    psi = pi;
end
Tf_d = @(eta,rho) a^3*psi*rhoF/2*rho.*W(rho).*H(eta).*besselj(n,eta.*rho)...
    .*(1+exp(-Hdown*2/a.*eta))./(1-exp(-Hdown*2/a.*eta));
        % kinetic energy of the fluid under the disk
Tf_u = @(eta,rho) a^3*psi*rhoF/2*rho.*W(rho).*H(eta).*besselj(n,eta.*rho)...
    .*(1+exp(-Hup*2/a.*eta))./(1-exp(-Hup*2/a.*eta));
        % kinetic energy of the fluid above the disk
Tf = @(eta,rho) Tf_d(eta,rho)+Tf_u(eta,rho);
        % total kinetic energy of the fluid
Td = @(rho) a^2*psi*rhoD*h/2*rho.*W(rho).^2;
        % kinetic energy of the disk
beta0 = integral2(Tf,0,Inf,b/a,1,'AbsTol',1e-2)/integral(Td,b/a,1,...
    'AbsTol',1e-4);
        % Added Virtual Mass Incremental factor
Gamma0 = beta0*rhoD/rhoF*h/a;
        % Nondimensionalized Added Virtual Mass Incremental factor
omegaB = [0;0];
for i = 1:2     % i=1 : n, i=2 : -n
    omegaB(i) = (sqrt(omegaA^2*(beta0+1)-beta0*(n*(1-K)*OmegaD)^2)...
        -beta0*n*(1-K)*OmegaD)/(beta0+1);
            % solving omega/sqrt(1+AVMI) when AVMI depends on omega;
            % here beta0 is actually AVMI factor when OmegaD = 0.
    n = -n;
end
omegaB      % co-rotating and counter-rotating waves frequency

%% OmegaD range plot
% plots analytical model results over a specified rotation speed range

%beta0 = 1;     % artificially redefines beta0 (for regime test)
nb = 51;        % number of ploted points
step = 1;       % rotation speed steps (in Hz)
speed = zeros(1,nb);        % rotation speeds
omega_an = zeros(2,nb);     % analytical results
omega_ce = zeros(1,nb);     % central value
```

```
for i = 1:nb
    speed(1,i) = (i-1)*step;    % from 0 to (nb-1)*step vector
    for j = 1:2
        omega_an(j,i) = (sqrt(omegaA^2*(beta0+1)-beta0*(n*(1-K)*...
            speed(1,i))^2)-beta0*n*(-1)^(j-1)*(1-K)*speed(1,i))/(beta0+1);
    end
    omega_ce(1,i) = mean(omega_an(:,i));
end

range0 = figure(2);
hold on
Aplot = plot(speed,omega_an,'-','color',[1 0.5 0],'linewidth',2);
Cplot = plot(speed,omega_ce,'-k','linewidth',2);
plot([0 (nb-1)*step],[omega_ce(1,1) omega_ce(1,1)],'--k')

%% Flutter instability
% plots analytical model results for omega > 0 and < 0 (n > 0), both Re
% and Im parts --> allows the detection of the critical speed for flutter
% instability.
nb = 1001;       % number of ploted points
step = 1;        % rotation speed steps (in Hz)
speed = zeros(1,nb);        % rotation speeds
omega_re = zeros(2,nb);     % analytical results, real part
omega_im = zeros(2,nb);     % analytical results, imaginary part
for i = 1:nb                % non-dimensionnal
    speed(1,i) = (i-1)*step/omegaA;    % from 0 to (nb-1)*step vector
    for j = 1:2
        omega_re(j,i) = real((-1)^j*(sqrt((beta0+1)-beta0*(n*...
            (1-K)*speed(1,i))^2)-beta0*n*(-1)^(j-1)*(1-K)*speed(1,i))/...
            (beta0+1));
        omega_im(j,i) = imag((-1)^j*(sqrt((beta0+1)-beta0*(n*...
            (1-K)*speed(1,i))^2)-beta0*n*(-1)^(j-1)*(1-K)*speed(1,i))/...
            (beta0+1));
    end
end
rangeF = figure(3);
```

```
subplot(2,1,1);
Fplot3 = plot(speed,omega_re,'k-','linewidth',1);
subplot(2,1,2);
plot(speed,omega_im,'k-','linewidth',1);

%% Stability map
% non-dimensional critical speed (flutter) plot for any mode
nb = 10001;          % number of ploted points
step = 0.01;         % beta0 steps
beta00 = zeros(1,nb);       % AVMI factors
omega_cr = zeros(1,nb);     % critical speeds (flutter) [-]
for i = 1:nb
    beta00(1,i) = (i-1)*step;    % from 0 to (nb-1)*step vector
    omega_cr(1,i) = sqrt(1+1/beta00(1,i));
end
stability = figure(4);
Splot = loglog(omega_cr,beta00,'-k','linewidth',2);

%% Forced response -- Dirac excitation -- no fluid
m = rhoD*h*pi*(a^2-b^2);    % mass of disk (kg)
r0 = a;                                % force application radius (m)
OmegaD = 10;                           % disk rotation freq. (Hz)
Omega = meshgrid(0:1:2*omegaA);        % excitation frequency (Hz)
xi = 0.1;                              % damping coefficient

F0 = r0*(A*besselj(n,k1*r0)+B*bessely(n,k1*r0)+C*besseli(n,k1*r0)+...
    D*besselk(n,k1*r0));    % force amplitude (N)
U = F0/8/pi/m*((pi^2*(omegaA^2-(Omega(1,:)+n*OmegaD).^2).^2+(xi*omegaA...
    .*(Omega(1,:)+n*OmegaD)).^2).^(-1/2)+(pi^2*(omegaA^2-(Omega(1,:)...
    -n*OmegaD).^2).^2+(xi*omegaA.*(Omega(1,:)-n*OmegaD)).^2).^(-1/2));
        % displacement amplitude (m)
OmegaR = Omega(1,find(U == max(U))) % max. amplitude resonance freq. (Hz)

forcedSin = figure(5);
plot(Omega(1,:),U,'k','linewidth',2)
```

APPENDIX B FORTRAN ROUTINE: INPUT PARAMETERS

This routine, inspired by the work of Trondal Svendsen and Michaelsen (2008), is used in the CFX model at the beginning of the simulation (`User Input` Junction Box routine option) to input parameters, create variables and prepare some domains where to stock information during the computation. More detailed information on each called function can be found in the CFX documentation. Code is in FORTRAN 77.

```
#include "cfx5ext.h"
dllexport(USR_INI)
      SUBROUTINE USR_INI ( CZ,DZ,IZ,LZ,RZ )
      IMPLICIT NONE
CC --------------------
CC  Writes data into the directory /USER_DATA, which is created when
CC  this Junction Box routine is called with the User Input option.
CC  NDOF = 2 (2 waves, rotor only), N = 3
CC=======================================================================
C     Preprocessor includes
C ------------------------------
#include "MMS.h"
#include "stack_point.h"
C ------------------------------
C        Argument list
C ------------------------------
      INTEGER IZ(*)
      CHARACTER CZ(*)*(1)
      DOUBLE PRECISION DZ(*)
      LOGICAL LZ(*)
      REAL RZ(*)
C ------------------------------
C        Local Parameters
C ------------------------------
      CHARACTER*(*) ROUTIN
      PARAMETER     (ROUTIN = 'USR_GET_TRNINFO')
C ------------------------------
```

```
C        Local Variables
C ------------------------------
      INTEGER N
      CHARACTER*4 CRESLT
      REAL DT, K, M
C ------------------------------
C        Stack pointers
C ------------------------------
      __stack_point__ pDT, pN, pK, pM
      __stack_point__ pZ, pZ0, pZD, pZD0, pZDD, pZDD0
C=======================================================================
C    Executable Statements
C --------------------------
C Initializing number of nodal diameters
      N = 3
C Initializing modal mass (kg) and stiffness (N/m)
C !! use modal parameters for considered disk !!
      K = 841475611d0
      M = 61.44d0
C Obtaining timestep size DT from MMS.
      CALL PEEKR('/FLOW/ALGORITHM/TRANS/DURATION/TSTEPS/VALUE',
     &           1,DT,'STOP',CRESLT,RZ)
C Putting current directory on top of stack and changing to USER_DATA.
      CALL PSHDIR( '/', 'STOP', CRESLT )
      CALL CHGDIR( 'USER_DATA', 'STOP', CRESLT )
C Allocating space for scalars (INTEGER)
      CALL MAKDAT( 'N'    , 'INTR', 'STOP', 1  , pN    , CRESLT)
C Allocating space for scalars (REAL).
      CALL MAKDAT( 'DT'   , 'REAL', 'STOP', 1  , pDT   , CRESLT)
      CALL MAKDAT( 'K'    , 'REAL', 'STOP', 1  , pK    , CRESLT)
      CALL MAKDAT( 'M'    , 'REAL', 'STOP', 1  , pM    , CRESLT)
C Reading scalar data into allocated space (INTEGER).
      CALL POKEI ( 'N'    , 1, N    , 'STOP', CRESLT, IZ )
C Reading scalar data into allocated space (REAL).
      CALL POKER ( 'DT'   , 1, DT   , 'STOP', CRESLT, RZ )
      CALL POKER ( 'K'    , 1, K    , 'STOP', CRESLT, RZ )
```

```
      CALL POKER ( 'M'    , 1, M    , 'STOP', CRESLT, RZ )
C Allocating space (corresponding to the number of DOF considered) for REAL
C arrays, and supplying stack pointers pVARIABLENAME.
      CALL MAKDAT ('Z'     ,'REAL', 'STOP', 2  , pZ    , CRESLT)
      CALL MAKDAT ('Z0'    ,'REAL', 'STOP', 2  , pZ0   , CRESLT)
      CALL MAKDAT ('ZD'    ,'REAL', 'STOP', 2  , pZD   , CRESLT)
      CALL MAKDAT ('ZD0'   ,'REAL', 'STOP', 2  , pZD0  , CRESLT)
      CALL MAKDAT ('ZDD'   ,'REAL', 'STOP', 2  , pZDD  , CRESLT)
      CALL MAKDAT ('ZDD0'  ,'REAL', 'STOP', 2  , pZDD0 , CRESLT)
C Initializing Z, Z0, DZ, DZ0, DDZ and DDZ0.
      CALL SET_A_0 (RZ(pZ)   ,2)
      CALL SET_A_0 (RZ(pZ0)  ,2)
      CALL SET_A_0 (RZ(pZD)  ,2)
      CALL SET_A_0 (RZ(pZD0) ,2)
      CALL SET_A_0 (RZ(pZDD) ,2)
      CALL SET_A_0 (RZ(pZDD0),2)
C
      CALL POPDIR( 'STOP', CRESLT )
C
      END SUBROUTINE USR_INI
```

APPENDIX C FORTRAN ROUTINE: RUNGE-KUTTA ALGORITHM

This routine, inspired by the work of Trondal Svendsen and Michaelsen (2008), is called in the CFX model at each time step of the simulation (`End of Time Step` Junction Box routine option) to compute the new maximum Z-displacement with the Runge-Kutta method (RK4) algorithm. More detailed information on each called function can be found in the CFX documentation. Code is in FORTRAN 77.

```
#include "cfx5ext.h"
dllexport(USR_RK4)
      SUBROUTINE USR_RK4( CZ,DZ,IZ,LZ,RZ )
      IMPLICIT NONE
CC --------------------
CC  Rotor mesh displacement prediction with RK4 algorithm for N=3
CC======================================================================
C     Preprocessor includes
C ------------------------------
#include "MMS.h"
#include "stack_point.h"
C ------------------------------
C        Argument list
C ------------------------------
      INTEGER IZ(*)
      CHARACTER CZ(*)*(1)
      DOUBLE PRECISION DZ(*)
      LOGICAL LZ(*)
      REAL RZ(*)
C ------------------------------
C        Local Variables
C ------------------------------
      INTEGER I, ISIZE, N
      INTEGER pZ, pZ0, pZD, pZD0
      REAL DT, M, K
      REAL K11, K21, K12, K22, K13, K23, K14, K24
      REAL F1, F2
```

```
      REAL FMOD(2)
      REAL Z(2), Z0(2), ZD(2), ZD0(2)
      CHARACTER*4 CRESLT, CDTYPE
C=======================================================================
C    Executable Statements
C --------------------------
C Loading 'REAL' variables from MMS.
      CALL PEEKR ( '/USER_DATA/DT'   , 1, DT   , 'STOP', CRESLT, RZ )
      CALL PEEKR ( '/USER_DATA/M'    , 1, M    , 'STOP', CRESLT, RZ )
      CALL PEEKR ( '/USER_DATA/K'    , 1, K    , 'STOP', CRESLT, RZ )
C Loading 'INTEGER' variable from MMS.
      CALL PEEKI ( '/USER_DATA/N'    , 1, N    , 'STOP', CRESLT, IZ )
C Calculating FMOD on rotor.
      CALL SET_A_0 (FMOD, 2)
C FMOD(1)=> COS(N*THETA); FMOD(2)=> SIN(N*THETA)
C Integration of the pressure field projection on the modeshape.
      CALL USER_GET_GVAR('m1discrot1FmodRePerAvar','rotor',
     &           'areaInt',CRESLT,FMOD(1),CZ,DZ,IZ,LZ,RZ)
      CALL USER_GET_GVAR('m1discrot1FmodImPerAvar','rotor',
     &           'areaInt',CRESLT,FMOD(2),CZ,DZ,IZ,LZ,RZ)
C Rebuilding FMOD on the entire disk surface.
      FMOD(1) = N*FMOD(1)
      FMOD(2) = N*FMOD(2)
C Locating Z, Z0, ZD and ZD0 from MMS.
      CALL LOCDAT('/USER_DATA/Z'    ,CDTYPE,'STOP',ISIZE,pZ    ,CRESLT)
      CALL LOCDAT('/USER_DATA/Z0'   ,CDTYPE,'STOP',ISIZE,pZ0   ,CRESLT)
      CALL LOCDAT('/USER_DATA/ZD'   ,CDTYPE,'STOP',ISIZE,pZD   ,CRESLT)
      CALL LOCDAT('/USER_DATA/ZD0'  ,CDTYPE,'STOP',ISIZE,pZD0  ,CRESLT)
C Initializing RUNGE-KUTTA by setting Z0=Z, ZD0=ZD.
      DO I=1,2
        RZ(pZ0+I-1)   = RZ(pZ+I-1)
        RZ(pZD0+I-1)  = RZ(pZD+I-1)
      END DO
C Calculating new displacement Z and velocity DZ.
      DO I=1,2
        K11 = DT*F1(RZ(pZD0+I-1))
```

```
        K21 = DT*F2(RZ(pZ0+I-1),FMOD(I),M,K)
        K12 = DT*F1(RZ(pZD0+I-1)+0.5*K21)
        K22 = DT*F2(RZ(pZ0+I-1)+0.5*K11,FMOD(I),M,K)
        K13 = DT*F1(RZ(pZD0+I-1)+0.5*K22)
        K23 = DT*F2(RZ(pZ0+I-1)+0.5*K12,FMOD(I),M,K)
        K14 = DT*F1(RZ(pZD0+I-1)+K23)
        K24 = DT*F2(RZ(pZ0+I-1)+K13,FMOD(I),M,K)
        RZ(pZ+I-1) = RZ(pZ0+I-1)+(K11+2*K12+2*K13+K14)/6
        RZ(pZD+I-1)= RZ(pZD0+I-1)+(K21+2*K22+2*K23+K24)/6
      END DO
      END SUBROUTINE USR_RK4
C=======================================================================
C Functions for Runge-Kutta algorithm
C PHI = Z, PSI = ZD, FMOD = FMOD(I)

      FUNCTION F1(PSI)
        REAL    F1
        REAL    PSI
        F1 = PSI
        RETURN
      END FUNCTION

      FUNCTION F2(PHI,FMOD,M,K)
        REAL    F2
        REAL    PHI,FMOD,M,K
        F2 = (FMOD-K*PHI)/M
        RETURN
      END FUNCTION
```

APPENDIX D FORTRAN ROUTINE: Z-DISPLACEMENT

This routine, inspired by the work of Trondal Svendsen and Michaelsen (2008), is called in the CFX model (User CEL Function) to load the computed maximum Z-displacement in CFX, so it can be used in CEL expressions. More detailed information on each called function can be found in the CFX documentation. Code is in FORTRAN 77.

```
#include "cfx5ext.h"
dllexport(USR_DISP_Z)
      SUBROUTINE USR_DISP_Z(
     &  NLOC, NRET, NARG, RET, ARGS, CRESLT, CZ,DZ,IZ,LZ,RZ )
      IMPLICIT NONE
C ------------------------------
C     Preprocessor includes
C ------------------------------
#include "MMS.h"
#include "stack_point.h"
C ------------------------------
C     Variables
C ------------------------------
      INTEGER NLOC,NARG,NRET
      CHARACTER*4 CRESLT, CDTYPE
      REAL ARGS(NLOC,NARG), RET(NLOC,NRET)
C
      INTEGER IZ(*)
      CHARACTER CZ(*)*(1)
      DOUBLE PRECISION DZ(*)
      LOGICAL LZ(*)
      REAL RZ(*)
C
      INTEGER ISIZE, I
C ------------------------------
C        Stack pointers
C ------------------------------
      __stack_point__ pZ
```

```
C=======================================================================
C    Executable Statements
C --------------------------
C Initializing RET to zero.
      CALL SET_A_0 (RET, NLOC*1)
C Loading Z from MMS.
      CALL LOCDAT('/USER_DATA/Z'  ,CDTYPE,'STOP', ISIZE, pZ ,CRESLT)
C Returning the correct Z, associated with the cosine or sine form
C ARGS=1 => Z_C; ARGS=2 => Z_S
      DO I=1,NLOC
        RET(I,1) = RZ(pZ+ARGS(1,1)-1)
      END DO
C Set success flag.
      CRESLT = 'GOOD'
C
      END SUBROUTINE USR_DISP_Z
```

APPENDIX E DISCUSSION ON THE HIGH FREQUENCY OSCILLATIONS

After a certain simulated time that depends on geometrical and numerical parameters, interfering high frequency oscillations appear and prevent the observation of the beating oscillation, and therefore of the split. Figure E.1 presents these oscillations parasitizing the q_c/a signal for different fluid compressibilities. Lowering the compressibility triggers the oscillations to appear sooner in the simulation, while increasing it delays them. The signal remains identical before the oscillations appear, regardless of the compressibility. Figure E.2 shows the fast Fourier transform of these q_c/a signals. The disk structural frequency does not depend on the compressibility, while the parasitic oscillations frequency is proportional to $\sqrt{B}$.

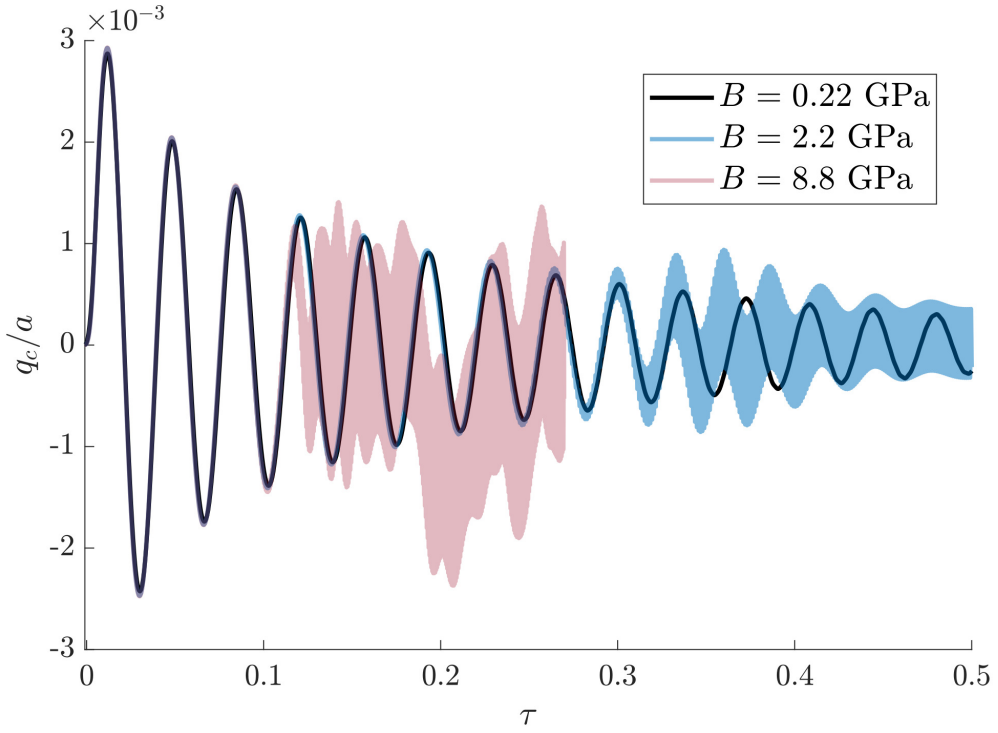

Figure E.1 q_c/a as a function of the elapsed dimensionless time for mode $n = 3$, $s = 0$ and the Presas et al. (2015) geometry. The compressibility is varied through the bulk modulus B. Water corresponds to $B = 2.2$ GPa. Increasing B reduces the compressibility and triggers the high frequency oscillations to appear sooner. Reducing B increases the compressibility and delays the high frequency oscillations. Before these appear, the q_c/a signals are identical, regardless of B.

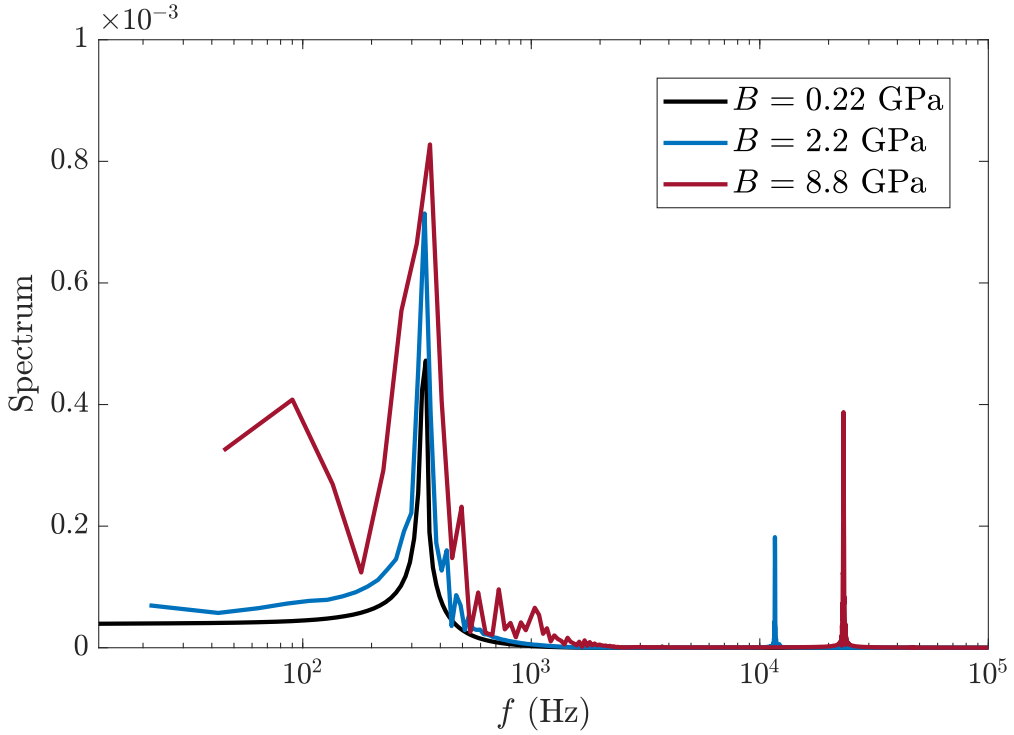

Figure E.2 Fast Fourier transform of the q_c/a signals shown in Figure E.1. The low frequency corresponds to the disk structural frequency, and does not depend on the value of the bulk modulus B. The high frequency corresponds to the parasitic oscillations, and is proportional to $\sqrt{B}$.

The bulk modulus B is linked to the sound speed in the fluid domain c by

$$c = \sqrt{B/\rho_F}\,. \tag{E.1}$$

This proves that the high frequency oscillations are acoustic vibrations, a different physics than for the mode split. Because the walls are perfectly reflective in the numerical model, the acoustic vibrations add up and hide the studied signal when their orders of magnitude are similar. However, because the structural frequency does not depend on B, choosing a low compressibility value delays the parasitic oscillations and allows the study of the q_c/a and q_s/a signals over sufficiently long periods of time. The black curve of Figure E.1 is a good example of how to avoid the acoustic parasitizing. Additionally using closely grouped monitor points on the disk surface also helps detect the beat in a shorter simulated physical time.